Mean-field approach to evolving spatial networks, with an application to osteocyte network formation

Jake P. Taylor-King,[1,2] David Basanta,[2] S. Jonathan Chapman,[1] and Mason A. Porter[3,1,4]
[1]*Mathematical Institute, University of Oxford, Oxford, OX2 6GG, United Kingdom*
[2]*Department of Integrated Mathematical Oncology, H. Lee Moffitt Cancer Center and Research Institute, Tampa, Florida 33612, USA*
[3]*Department of Mathematics, University of California Los Angeles, Los Angeles, California 90095, USA*
[4]*CABDyN Complexity Centre, University of Oxford, Oxford, OX1 1HP, United Kingdom*
(Received 28 January 2017; published 5 July 2017)

We consider evolving networks in which each node can have various associated properties (a state) in addition to those that arise from network structure. For example, each node can have a spatial location and a velocity, or it can have some more abstract internal property that describes something like a social trait. Edges between nodes are created and destroyed, and new nodes enter the system. We introduce a "local state degree distribution" (LSDD) as the degree distribution at a particular point in state space. We then make a mean-field assumption and thereby derive an integro-partial differential equation that is satisfied by the LSDD. We perform numerical experiments and find good agreement between solutions of the integro-differential equation and the LSDD from stochastic simulations of the full model. To illustrate our theory, we apply it to a simple model for osteocyte network formation within bones, with a view to understanding changes that may take place during cancer. Our results suggest that increased rates of differentiation lead to higher densities of osteocytes, but with a smaller number of dendrites. To help provide biological context, we also include an introduction to osteocytes, the formation of osteocyte networks, and the role of osteocytes in bone metastasis.

DOI: 10.1103/PhysRevE.96.012301

I. INTRODUCTION

Networks, in which entities ("nodes") interact with each other via "edges," are a useful representation of complex systems [1]. They have often been very helpful for formulating and answering questions in biology, sociology, engineering, and numerous other fields. Because the present work is motivated by a biological application, let's consider a few examples from biology. Many systems—such as blood vasculature [2], leaf venation [3], and fungi [4,5]—can be treated as biological transportation networks, in which edges carry resources and nodes operate as junctions. Some of these studies exploit ideas from fluid mechanics and energy minimization to investigate flow through various media [4,6–8]. To give another type of example, in evolutionary game theory, a node can represent a biological agent, and edges indicate interactions in a "game" between those agents [9]. Applications range from behavioral ecology [10] to investigating tumor heterogeneity in cancer [11]. Changes in node fitness can depend on, for example, a node's phenotype and its immediate neighbors [12].

Many of the above examples involve "spatial networks" [13], and spatial constraints can exert significant influence (directly and/or indirectly) on both network structure and function. In the aforementioned examples, the networks are embedded in space, and one thus can assign physical locations to the nodes and edges. This is clearly important when considering dynamical processes (such as biological contagions [14]) on those networks [15].

Some spatial networks grow in time as they form: new nodes and edges can join a spatial network, and the spatial domain can expand. For example, cities often grow outwards or arise when borders from multiple settlements coalesce [16–18]. Fungi, which are living networks, expand to reach nutrients, and such growth induces flows of mass [4,5].

In the present paper, we propose a framework for describing evolving spatial networks. We then apply this framework to examine the formation of osteocyte networks in bone (see Fig. 8 for a schematic). During bone formation, cells called osteoblasts secrete bone matrix and differentiate into cells called osteocytes, and the ensuing growth process results in a network of connected cells that communicate by chemical diffusion via gap junctions [19–22]. In Sec. VII, we develop and analyze a model for this process, with the motivation of using network analysis to study bone cancer. In pathological bone, the highly regulated bone-remodeling signaling pathway is disrupted, and it may be possible to gain insight into the nature of this disruption using tools from network analysis. See Ref. [23] for a recent paper on osteocyte networks.

There are myriad models of network formation [1]. There are at least three possible ways of formulating such a model: (1) all nodes and edges are created simultaneously with a single algorithmic step (e.g., a graph created from the Erdős–Rényi (ER) random-graph model $G(n,p)$ [1] or a standard random geometric graph [24]); (2) nodes and edges have an implicit order of creation but time is not considered explicitly (e.g., in some preferential-attachment models [25,26]); or (3) nodes and edges have an order of creation and time is considered explicitly (e.g., in some preferential-attachment models [27,28] and in adaptive network models [29]). Because we want to incorporate time explicitly, we will consider spatial networks in category (3) in the present paper. See also the recent work by Zuev *et al.* on geometric preferential-attachment models [30].

When studying a model in category (3), it is common to employ kinetic approximations [27,28,31,32]. Such approximations often allow one to construct a "master equation" to obtain approximate and/or asymptotic expressions for quantities such as degree distributions, component sizes, and cycle sizes [31]. These equations can take the form of an ordinary differential

equation (ODE), partial differential equation (PDE), or other continuous model. By carefully constructing a general state space of the system, we derive an extension to the ODE master equations given in Refs. [27,28,31,32] to obtain a master equation in the form of an integro-partial differential equation (IPDE) that incorporates this state space.

Our work illustrates how to use a master-equation approach to study spatial networks. As an illustration of its potential, we examine degree distributions in a very general model of evolving spatial networks and use our results to gain insights into osteocyte network formation in bone. An important benefit of using an explicit time-dependent kinetic approach is that it allows one to incorporate nodes that move through a state space (e.g., particles that diffuse). Note that we will often use the terms "nodes" and "particles" interchangeably (depending on the context). When considering spatially embedded network models, the state space corresponds to each node being located in a copy of the physical space. From a mathematical viewpoint, our approach is reminiscent of some models of social networks [33,34], for which the state space corresponds to a latent social space described by some internal parameters; however, these models have no time dependence. See also the recent paper [35] on macroscopic descriptions for particle interactions mediated by time-dependent networks.

The remainder of our paper is organized as follows. In Sec. II, we define the concept of a "local state degree distribution" (LSDD), which encapsulates the degree distribution of a network near a point in state space. In Sec. III, we give a description of our model of evolving spatial networks. In Sec. IV, we derive an equation for the LSDD when edges are created but cannot be destroyed. In Sec. V, we incorporate edge destruction into our model. Our derivations require approximations, so we use numerical simulations to explore agreement and discrepancies between theory and our derived equations in Sec. VI. In Sec. VII, we use our model for evolving spatial networks to formulate a model for osteocyte network formation. We conclude and discuss future directions in Sec. VIII. In appendices, we give additional details on derivations and numerical implementations.

II. A LOCAL STATE DEGREE DISTRIBUTION

We consider networks in which each node (i.e., particle) has some number of associated properties in addition to those, such as degree distribution, that arise from network structure. For example, each node may have a spatial location and a velocity, or it may have some more abstract internal ("latent") property describing, for example, some social trait. We collect these properties together into a state vector $\boldsymbol{s}$, which belongs to a state space $\mathbb{S}$.

The density $f(t,\boldsymbol{s})$ of particles in the state space gives the expected number of particles with state $\boldsymbol{s}$ [36]. As is well-appreciated, a common way to study the properties of models of network formation is to examine the degree distribution [1]. In this paper, we combine these ideas to consider what we call a *local state degree distribution* (LSDD) $u_k(t,\boldsymbol{s})$, which gives the expected number of particles of degree k at time t with state vector $\boldsymbol{s}$. One can write the LSDD as

$$u_k(t,\boldsymbol{s}) = p_k(t \mid \boldsymbol{s}) f(t,\boldsymbol{s}),$$

where $p_k(t \mid \boldsymbol{s})$ is the conditional probability that a node at time t has degree k, given that its state is $\boldsymbol{s}$. We can recover both f and p_k from u_k via

$$f(t,\boldsymbol{s}) = \sum_{k=0}^{\infty} u_k(t,\boldsymbol{s}), \quad p_k(t \mid \boldsymbol{s}) = \frac{u_k(t,\boldsymbol{s})}{\sum_{k=0}^{\infty} u_k(t,\boldsymbol{s})}. \tag{1}$$

The degree distribution of the whole network is given by

$$P_k(t) = \frac{\int_{\mathbb{S}} u_k(t,\boldsymbol{s})\, d\boldsymbol{s}}{\sum_{k=0}^{\infty} \int_{\mathbb{S}} u_k(t,\boldsymbol{s})\, d\boldsymbol{s}}. \tag{2}$$

III. MODEL OF EVOLVING SPATIAL NETWORKS

We now present a model for evolving spatial networks. Our model has three tunable features. First, edges can be created and deleted. Second, new nodes can be created (but we do not allow node deletion). Finally, we specify a model (possibly depending on network structure) for the evolution of the state $\boldsymbol{s}$ of each node.

Suppose at time t that there are $N(t)$ nodes with state vectors $\boldsymbol{s}_i$ and degrees k_i (with $i \in \{1,\ldots,N\}$). We also suppose that new edges are created between each pair of nodes as independent Poisson processes, where $\mathcal{C}(\boldsymbol{s}_i,k_i,\boldsymbol{s}_j,k_j)$ is the rate of edge creation between node i and node j, so that the probability of an edge being created between node i and node j between times t and $t+dt$ is $\mathcal{C}(\boldsymbol{s}_i,k_i,\boldsymbol{s}_j,k_j)\,dt$. We also suppose that $\mathcal{C}$ depends on the states and degrees of the two nodes i and j, but that it does not depend on other properties of the network (such as whether an edge between node i and node j already exists). Thus, our model allows *multiedges* (i.e., multiple edges between two distinct nodes).

Similarly, we suppose that existing nodes are deleted as independent Poisson processes, where $\mathcal{D}(\boldsymbol{s}_i,k_i,\boldsymbol{s}_j,k_j)$ is the rate of edge deletion (per edge) between node i and node j. We also suppose that new particles, which have degree 0, arrive randomly via a Poisson process with constant rate $\mathcal{J}$, and we assign to them a state drawn at random from the probability distribution $\mathcal{P}$.

The final component of our model is the equation of motion of the particles in the state space. Many possible models (both deterministic and stochastic) are available, and we want to keep our presentation as general as possible. Nevertheless, it is useful to have a model in mind to fix ideas, and we thus present several examples.

The simplest case is for each node to have a constant state vector. Our first nontrivial example consists of identical particles of mass $m > 0$ that follow Newton's equations of motion with a smooth pairwise potential Φ. In that case, $\boldsymbol{s}_i(t) = (\boldsymbol{x}_i(t),\boldsymbol{v}_i(t)) \in \mathbb{S} \subseteq \mathbb{R}^{2d}$ and

$$\dot{\boldsymbol{x}}_i = \boldsymbol{v}_i, \quad m\dot{\boldsymbol{v}}_i = -\sum_{\substack{j=1 \\ j\neq i}}^{n} \nabla_{\boldsymbol{x}_i} \Phi(\boldsymbol{x}_i - \boldsymbol{x}_j). \tag{3}$$

Variations of these equations have been used to consider collective motion such as swarming [37–39]. Our second example consists of the stochastic position jump process in which $\boldsymbol{s}_i(t) = \boldsymbol{X}_i(t) \in \mathbb{S} \subset \mathbb{R}^d$ and [40]

$$d\boldsymbol{X}_i = \boldsymbol{\mu}(\boldsymbol{X}_i)\,dt + \sigma\; d\boldsymbol{W}_t, \tag{4}$$

TABLE I. Model description: (a) edge creation, (b) edge deletion, (c) node creation, and (d) evolution of node state.

(a) The rate of edge creation between nodes i and j is $\mathcal{C}(\boldsymbol{s}_i,k_i,\boldsymbol{s}_j,k_j)$.
(b) The rate of edge deletion per edge between nodes i and j is $\mathcal{D}(\boldsymbol{s}_i,k_i,\boldsymbol{s}_j,k_j)$.
(c) Nodes of degree 0 enter the system at rate $\mathcal{J}$. We assign the new node a state $\boldsymbol{s}^* \in \mathbb{S}$, where we draw $\boldsymbol{s}^*$ from the distribution $\mathcal{P}$.
(d) Nodes move in the state space $\mathbb{S}$ according to some (possibly stochastic) differential equation. We specify a single differential equation for each node, and all nodes must follow the same differential equation.

where $\boldsymbol{W}_t$ is standard Brownian motion (i.e., a Wiener process) [41]. Other stochastic examples include velocity-jump processes [42] and fractional diffusion processes [43].

In each of the above examples, the motion in state space is independent of network structure. Of course, it is also possible to imagine scenarios in which the motion depends on node degree or other structural features.

We summarize the model events and state update in Table I, and we illustrate them in Fig. 1. Our model treats all nodes identically, although our methodology can be extended to heterogeneous classes of nodes or heterogeneous classes of edges. (Both of these generalizations are examples of multilayer networks [44].) To consider such cases, one can modify the kinetic methodology from Refs. [45,46].

IV. MODEL ANALYSIS: NO EDGE DELETION

We begin by considering the case in which there is no edge deletion; that is, $\mathcal{D}(\boldsymbol{s}_i,k_i,\boldsymbol{s}_j,k_j) = 0$ for all $\boldsymbol{s}_i,k_i,\boldsymbol{s}_j,k_j$. In the next subsection, we give a set of hierarchical master Fokker–Planck (FP) equations for the probability distribution of the state of the system. Because it is not pragmatic to work in this high-dimensional space, in Sec. IV B, we reduce the dimension using mean-field arguments from kinetic theory.

A. Fokker–Planck equation

We define $\mathcal{F}_n^{\vec{k}_n}(t,\vec{s}_n)$ to be the probability that a network has n nodes with degree sequence $\vec{k}_n = \{k_1,\ldots,k_n\}$ and state vectors $\vec{s}_n = \{\boldsymbol{s}_1,\ldots,\boldsymbol{s}_n\}$. Note the normalization

$$\sum_{n=0}^{\infty}\left\{\sum_{K_{1,n}}\left[\int_{\mathbb{S}^n}\mathcal{F}_n^{\vec{k}_n}(t,\vec{s}_n)\,d\vec{s}_n\right]\right\} = 1, \tag{5}$$

where $K_{a,b}$ is shorthand for summing over all possible degrees for nodes $i \in \{a,a+1,\ldots,b\}$; that is,

$$\sum_{K_{a,b}} \equiv \sum_{k_a=0}^{\infty}\sum_{k_{a+1}=0}^{\infty}\cdots\sum_{k_b=0}^{\infty}. \tag{6}$$

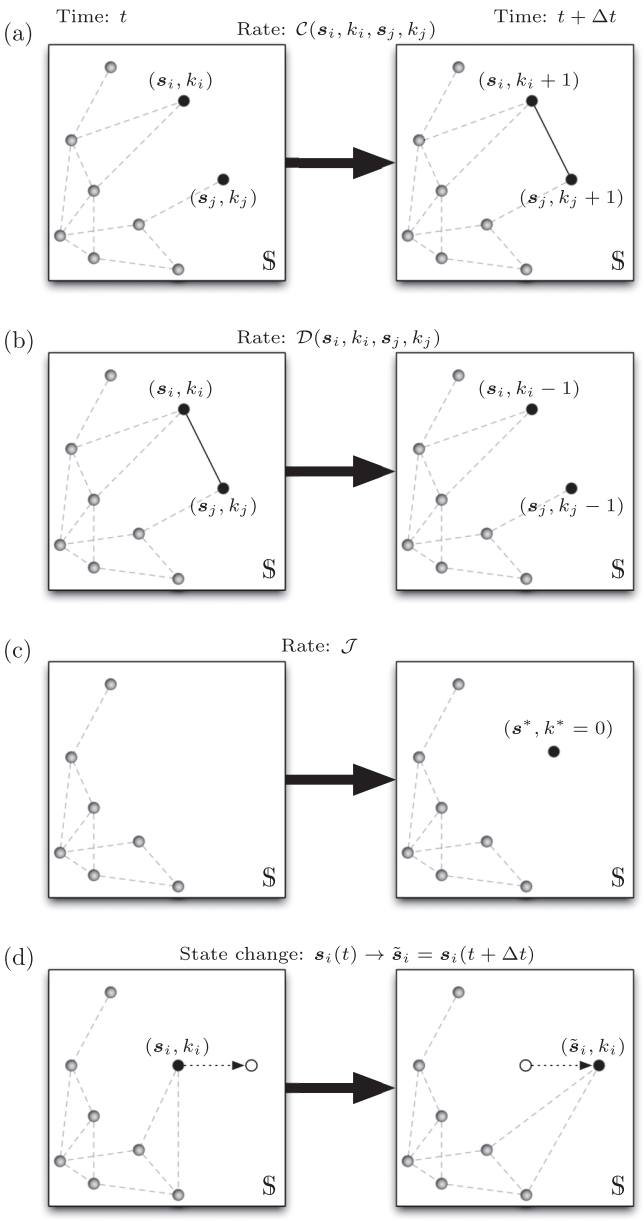

FIG. 1. Diagrammatic illustration of our model of evolving spatial networks. In each panel, the square box represents the state space $\mathbb{S}$. In each time step of size Δt (where $0 < \Delta t \ll 1$), the following events can occur: (a) edge creation, (b) edge deletion, (c) node creation, and (d) evolution of node state.

We are not considering edge deletion and we have assumed that edge creation and state-space motion depend only on node state and degree, so it is possible to write a closed equation for $\mathcal{F}_n^{\vec{k}_n}(t,\vec{s}_n)$. In contrast, when we do consider edge deletion in Sec. V, it will not be enough simply to keep track of node degrees. We will need the full adjacency matrix.

Because the probability density function $\mathcal{F}_n^{\vec{k}_n}(t,\vec{s}_n)$ depends on the number of particles in the system (which changes when new nodes are created), we obtain a hierarchy of Fokker–Planck equations as in Ref. [47]. By considering a small time step

from t to $t+dt$ and partitioning over the events that can occur, we obtain

$$\left(\frac{\partial}{\partial t}+\mathcal{L}^{(n)}\right)\mathcal{F}_n^{\vec{k}_n}(t,\vec{s}_n)=\sum_{i=1}^{n}\sum_{j=i+1}^{n}\left[\mathcal{C}(\boldsymbol{s}_i,k_i-1,\boldsymbol{s}_j,k_j-1)\mathcal{F}_n^{\vec{k}_{n,-}^{i,j}}(t,\vec{s}_n)-\mathcal{C}(\boldsymbol{s}_i,k_i,\boldsymbol{s}_j,k_j)\mathcal{F}_n^{\vec{k}_n}(t,\vec{s}_n)\right]$$
$$+\sum_{i=1}^{n}\frac{1}{n}\delta_{k_i,0}\,\mathcal{J}\,\mathcal{P}(\boldsymbol{s}_i)\mathcal{F}_{n-1}^{\vec{k}_n^{i-}}\left(t,\vec{s}_n^{i-}\right)-\mathcal{J}\mathcal{F}_n^{\vec{k}_n}(t,\vec{s}_n)\,. \tag{7}$$

The operator on the left-hand side of Eq. (7) describes the evolution of particles in state space, and it depends on the particular model that one chooses for this evolution. For example, if nodes move according to Eq. (3), one has the Liouville flux term

$$\mathcal{L}^{(n)}\mathcal{F}_n^{\vec{k}_n}=\sum_{i=1}^{n}\left[\boldsymbol{v}_i\cdot\nabla_{\boldsymbol{x}_i}+\frac{\boldsymbol{F}(\vec{x}_n)}{m}\cdot\nabla_{\boldsymbol{v}_i}\right]\mathcal{F}_n^{\vec{k}_n}, \tag{8}$$

where $\vec{x}_n=(\boldsymbol{x}_1,\ldots,\boldsymbol{x}_n)$ and

$$\boldsymbol{F}(\vec{x}_n)=-\sum_{\substack{j=1\\ j\neq i}}^{n}\nabla_{\boldsymbol{x}_i}\Phi(\boldsymbol{x}_i-\boldsymbol{x}_j)\,.$$

Alternatively, if $\boldsymbol{s}_i(t)$ evolves according to the stochastic differential equation (SDE) (4), one has the Kolmogorov forward operator

$$\mathcal{L}^{(n)}\mathcal{F}_n^{\vec{k}_n}=\sum_{i=1}^{n}\nabla_{\boldsymbol{x}_i}\cdot\left[\boldsymbol{\mu}(\boldsymbol{x}_i)-\frac{\sigma^2}{2}\nabla_{\boldsymbol{x}_i}\right]\mathcal{F}_n^{\vec{k}_n}. \tag{9}$$

If the states of nodes are time-independent, then $\mathcal{L}^{(n)}\equiv 0$.

The first term in parentheses on the right-hand side of Eq. (7) corresponds to edge-creation events between each pair, i and j, of nodes. The positive term corresponds to gaining a network with degree sequence $\vec{k}_n=\{k_1,\ldots,k_n\}$ from a network with degree sequence $\vec{k}_{n,-}^{i,j}=\{k_1,\ldots,k_i-1,\ldots,k_j-1,\ldots,k_n\}$ by adding an edge between nodes i and j. The negative term corresponds to losing a network of degree sequence $\vec{k}_n$ (as it changes to a network of degree sequence $\vec{k}_{n,+}^{i,j}=\{k_1,\ldots,k_i+1,\ldots,k_j+1,\ldots,k_n\}$) by adding an edge between nodes i and j.

The second term on the right-hand side of Eq. (7) corresponds gaining a network with degree sequence $\{k_1,\ldots,k_{i-1},0,k_{i+1},\ldots,k_n\}$ from a network with degree sequence $\vec{k}_n^{i-}=\{k_1,\ldots,k_{i-1},k_{i+1},\ldots,k_{n-1}\}$ by adding a new node (of degree 0) to the system. The Kronecker delta $\delta_{k_i,0}$ ensures that this term is present only when $k_i=0$, corresponding to the new node having degree 0. One draws the new state $\boldsymbol{s}_i$ from the probability distribution with density function $\mathcal{P}$. (The state vector of the existing nodes is $\vec{s}_n^{i-}=(\boldsymbol{s}_1,\ldots,\boldsymbol{s}_{i-1},\boldsymbol{s}_{i+1},\ldots,\boldsymbol{s}_n)$.) We assign the label of the new node uniformly at random from the set $\{1,\ldots,n\}$ (rather than assigning it to be the last node n) to ensure that particles are indistinguishable.

The final term on the right-hand side of Eq. (7) describes the loss of a network with degree sequence $\vec{k}_n$ because of the addition of a new node. (One obtains a network with degree sequence $\{k_1,\ldots,k_{i-1},0,k_i,\ldots,k_n\}$ for some i.)

To save us from writing down separate equations for each case in which $k_i=0$ for some i (because it is impossible to arrive at a state in which a node has degree 0 by adding an edge to a state in which it has degree -1), we use the convention that $\mathcal{F}_n^{\vec{k}_n}(t,\vec{s}_n)=0$ if $n<0$ or $k_i<0$ for all $i\in\{0,1,\ldots,n\}$. We also suppose that particles are indistinguishable initially, so the initial condition $\mathcal{F}_n^{\vec{k}_n}(0,\vec{s}_n)$ is invariant with respect to index permutation. Equation (7) then ensures that this is true for all t.

It is not feasible to solve Eq. (7) analytically (except perhaps when the node state vectors are uncorrelated), and it is not practical to solve it numerically due to the high dimension of the domain. In Sec. IV B, we reduce the dimension of Eq. (7) using mean-field approaches from kinetic theory.

B. Low-dimensional approximation

To derive a low-dimensional approximation, we adapt methods from kinetic theory [37,48]. We keep the presentation brief in this subsection; we give more details in Appendix B.

A common approach in kinetic theory is to average over the states of particles 2 to n to find an equation for the marginal distribution function of the first particle [49,50] (the so-called "1-particle distribution function"). Because particles are indistinguishable, multiplying by n gives the probability of finding *any* particle in a given state. Here we adopt the same approach, and we average over the states and degrees of particles 2 to n. Because the number of particles itself can vary, we also need to average over this quantity. The resulting one-particle distribution function is exactly the previously defined LSDD $u_k(t,\boldsymbol{s})$. Specifically,

$$\begin{aligned}u_{k_1}(t,\boldsymbol{s}_1)&=\sum_{n=0}^{\infty}n\sum_{K_{2,n}}\int_{\mathbb{S}^{n-1}}\mathcal{F}_n^{\vec{k}_n}(t,\vec{s}_n)\,d\vec{s}_n^{(2)}\\&=\sum_{n=0}^{\infty}n\sum_{k_2=0}^{\infty}\cdots\sum_{k_n=0}^{\infty}\int_{\mathbb{S}^{n-1}}\mathcal{F}_n^{\vec{k}_n}(t,\boldsymbol{s}_1,\ldots,\boldsymbol{s}_n)\,d\boldsymbol{s}_2\ldots d\boldsymbol{s}_n,\end{aligned} \tag{10}$$

where we introduce the shorthand notation $d\vec{s}_n^{(\mu)}=d\boldsymbol{s}_\mu\ldots d\boldsymbol{s}_n$ for $\mu\in\{1,\ldots,n\}$. To find the equation satisfied by $u_k(t,\boldsymbol{s}_1)$, we apply the same summation and integration to the Fokker–Planck equation (7).

Because the summation and integration commutes with the time derivative, it follows for the first term on the left-hand side (LHS) of Eq. (7) that

$$\sum_{n=0}^{\infty}n\sum_{K_{2,n}}\int_{\mathbb{S}^{n-1}}\frac{\partial\mathcal{F}_n^{\vec{k}_n}(t,\vec{s}_n)}{\partial t}\,d\vec{s}_n^{(2)}=\frac{\partial u_{k_1}(t,\boldsymbol{s}_1)}{\partial t}\,. \tag{11}$$

For the next term on the LHS, we need to evaluate

$$\sum_{n=0}^{\infty} n \sum_{K_{2,n}} \int_{\mathbb{S}^{n-1}} \mathcal{L}^{(n)} \mathcal{F}_n^{\vec{k}_n} \, d\vec{s}_n^{(2)}. \tag{12}$$

If there are no interactions between particles in the state space, this term evaluates to $\mathcal{L}^{(1)} u_{k_1}$. Thus, for example, if $\mathcal{L}^{(n)}$ is given by (9), then this term is

$$\mathcal{L}^{(1)} u_{k_1} = \nabla_{\boldsymbol{x}_1} \cdot \left[\boldsymbol{\mu}(\boldsymbol{x}_1) - \frac{\sigma^2}{2} \nabla_{\boldsymbol{x}_1} \right] u_{k_1}. \tag{13}$$

When there are pairwise interactions between particles in the state space, for each interacting pair, one can perform the integration over all other particles. Consequently, after relabelling, one can write (12) in terms of the two-particle LSDD:

$$u^{(2)}_{k_1,k_2}(t,\boldsymbol{s}_1,\boldsymbol{s}_2) = \sum_{n=0}^{\infty} n(n-1) \sum_{K_{3,n}} \int_{\mathbb{S}^{n-2}} \mathcal{F}_n^{\vec{k}_n}(t,\vec{s}_n) \, d\vec{s}_n^{(3)}. \tag{14}$$

We do not have a closed equation for u_{k_1}, but we examine the first in a hierarchy of coupled equations (the BBGKY hierarchy) for the n-particle LSDDs ($n = 1,2,\ldots$). In this case, we make the common mean-field closure assumption that

$$u^{(2)}_{k_1,k_2}(t,\boldsymbol{s}_1,\boldsymbol{s}_2) \approx u_{k_1}(t,\boldsymbol{s}_1) u_{k_2}(t,\boldsymbol{s}_2). \tag{15}$$

For example, if $\mathcal{L}^{(n)}$ is given by Eq. (8), then (12) becomes

$$\bar{\mathcal{L}}^{(1)} u_{k_1} = \boldsymbol{v}_1 \cdot \nabla_{\boldsymbol{x}_1} u_{k_1} - \mathcal{B}\big(f, u_{k_1}\big), \tag{16}$$

where $\mathcal{B}(f,u_{k_1})$ is the mean-field approximation

$$\mathcal{B}(f,u_{k_1}) = \left(\nabla_{\boldsymbol{x}_1} \Phi * \int_{\mathbb{R}^d} f \, d\boldsymbol{v}_1 \right) \cdot \big(\nabla_{\boldsymbol{v}_1} u_{k_1} \big), \tag{17}$$

where $*$ represents the convolution operator and the function f is given in Eq. (1).

We now apply the same integration and summation to the right-hand side (RHS) of Eq. (7). We give a detailed derivation in Appendix B. Here we simply note that by relabelling particles and again using the fact that $\mathcal{F}_n^{\vec{k}_n}(t,\vec{s}_n)$ is invariant with respect to index permutation, we find that

$$\text{RHS} = \int_{\mathbb{S}} \sum_{k_2=0}^{\infty} \left[\mathcal{C}(\boldsymbol{s}_1,k_1-1,\boldsymbol{s}_2,k_2-1) u^{(2)}_{k_1-1,k_2-1}(t,\boldsymbol{s}_1,\boldsymbol{s}_2) - \mathcal{C}(\boldsymbol{s}_1,k_1,\boldsymbol{s}_2,k_2) u^{(2)}_{k_1,k_2}(t,\boldsymbol{s}_1,\boldsymbol{s}_2) \right] d\boldsymbol{s}_2 + \mathcal{JP}(\boldsymbol{s}_1)\delta_{k_1,0}. \tag{18}$$

We again need to use the mean-field closure assumption (15) to write the two-particle LSDD in terms of the one-particle LSDD. This gives the final closed mean-field equation for the one-particle LSDD in the absence of edge deletion:

$$\begin{aligned} \left[\frac{\partial}{\partial t} + \mathcal{L}^{(1)} \right] u_{k_1}(t,\boldsymbol{s}_1) = & \left[\int_{\mathbb{S}} \sum_{k_2=0}^{\infty} \mathcal{C}(\boldsymbol{s}_1,k_1-1,\boldsymbol{s}_2,k_2-1) u_{k_2-1}(t,\boldsymbol{s}_2) \, d\boldsymbol{s}_2 \right] u_{k_1-1}(t,\boldsymbol{s}_1) \\ & - \left[\int_{\mathbb{S}} \sum_{k_2=0}^{\infty} \mathcal{C}(\boldsymbol{s}_1,k_1,\boldsymbol{s}_2,k_2) u_{k_2}(t,\boldsymbol{s}_2) \, d\boldsymbol{s}_2 \right] u_{k_1}(t,\boldsymbol{s}_1) + \mathcal{JP}(\boldsymbol{s}_1)\delta_{k_1,0}, \end{aligned} \tag{19}$$

where $u_{k_1} \equiv 0$ if $k_1 < 0$ by convention. When $\mathcal{C}$ is a constant and $\mathbb{S}$ is a point, Eq. (19) reduces to the master equations given in Ref. [31]. The quadratic terms in Eq. (19) are analogous to the mean-field term in the Vlaslov equation, where a test particle feels the effect of a "cloud" of points [38,49,50].

V. DERIVATION OF THE MODEL: EDGE DELETION

The state space $\{(\vec{s}_n,\vec{k}_n) : n > 0\}$ that we used in Sec. IV is not sufficient when we allow edge deletion. With edge deletion, it is crucial to know whether an edge exists between each pair of nodes, so we must consider the underlying adjacency matrix. For undirected networks with multiedges, the adjacency matrix $A_n = A_n^T$ has entries $(A_n)_{ij}$ for $i \neq j$ and $i,j \in \{1,\ldots,n\}$, where $(A_n)_{ij} \in \mathbb{N}_0$ gives the number of edges between nodes i and j. (When necessary for clarity, we will write $(A_n)_{i,j}$.)

Because we consider probability distributions over A_n, the most efficient representation is to restrict attention to the independent entries of A_n. We thus change convention slightly and set $(A_n)_{ij} = 0$ for $i \geqslant j$; we will retain the term "adjacency matrix" to indicate the resulting matrix.

Let $\mathscr{F}_n^{A_n}(t,\vec{s}_n)$ denote the probability that a network has adjacency matrix A_n and n nodes with state vectors $\vec{s}_n = \{\boldsymbol{s}_1,\ldots,\boldsymbol{s}_n\}$. The normalization condition is

$$\sum_{n=1}^{\infty} \left\{ \sum_{A_n \in S_n} \left[\int_{\mathbb{S}^n} \mathscr{F}_n^{A_n}(t,\vec{s}_n) \, d\vec{s}_n \right] \right\} = 1, \tag{20}$$

where

$$S_n = \left\{ A_n : \begin{array}{ll} (A_n)_{ij} \in \mathbb{N}_0, & 1 \leqslant i < j \leqslant n \\ (A_n)_{ij} = 0, & \text{otherwise} \end{array} \right\}, \tag{21}$$

so that

$$\sum_{A_n \in S_n} \equiv \sum_{(A_n)_{12}=0}^{\infty} \cdots \sum_{(A_n)_{1n}=0}^{\infty} \sum_{(A_n)_{23}=0}^{\infty} \cdots \sum_{(A_n)_{n-1,n}=0}^{\infty}.$$

For fixed n, one can calculate the degree k_i of node i from the adjacency matrix using

$$k_i = \sum_{j=i+1}^{n} (A_n)_{ij} + \sum_{j=1}^{i-1} (A_n)_{ji}.$$

Therefore, we can relate the distributions $\mathcal{F}$ and $\mathscr{F}$ via

$$\mathcal{F}_n^{\vec{k}_n}(t,\vec{s}_n) = \sum_{A_n \in S_n} \left[\prod_{i=1}^{n} \delta\left(k_i, \sum_{j=i+1}^{n} (A_n)_{ij} + \sum_{j=1}^{i-1} (A_n)_{ji} \right) \right] \mathscr{F}_n^{A_n}(t,\vec{s}_n)\,, \tag{22}$$

where $\delta(a,b)$ is the Kronecker delta (which is usually written as δ_{ab}). When we include edge deletion, the hierarchical Fokker–Planck equation (7) becomes

$$\begin{aligned}\left(\frac{\partial}{\partial t} + \mathcal{L}^{(n)}\right)\mathscr{F}_n^{A_n}(t,\vec{s}_n) &= \sum_{i=1}^{n}\sum_{j=i+1}^{n} \mathcal{C}(\boldsymbol{s}_i,k_i-1,\boldsymbol{s}_j,k_j-1)\mathscr{F}_n^{A_{n,-}^{ij}}(t,\vec{s}_n) - \mathcal{C}(\boldsymbol{s}_i,k_i,\boldsymbol{s}_j,k_j)\mathscr{F}_n^{A_n}(t,\vec{s}_n) \\ &+ \sum_{i=1}^{n}\sum_{j=i+1}^{n} [(A_n)_{ij}+1]\mathcal{D}(\boldsymbol{s}_i,k_i+1,\boldsymbol{s}_j,k_j+1)\mathscr{F}_n^{A_{n,+}^{ij}}(t,\vec{s}_n) - (A_n)_{ij}\mathcal{D}(\boldsymbol{s}_i,k_i,\boldsymbol{s}_j,k_j)\mathscr{F}_n^{A_n}(t,\vec{s}_n) \\ &+ \frac{1}{n}\sum_{i=1}^{n}\left[\prod_{j=1}^{i-1}\delta(0,(A_n)_{ji})\right]\left[\prod_{j=i+1}^{n}\delta(0,(A_n)_{ij})\right]\mathcal{J}\mathcal{P}(\boldsymbol{s}_i)\mathscr{F}_{n-1}^{A_n^{i-}}\left(t,\vec{s}_n^{\,i-}\right) - \mathcal{J}\mathscr{F}_n^{A_n}(t,\vec{s}_n)\,,\end{aligned} \tag{23}$$

where

$$\left(A_{n,\pm}^{ij}\right)_{lm} = \begin{cases} (A_n)_{lm} \pm 1, & \text{if } (i,j) = (l,m)\,, \\ (A_n)_{lm}, & \text{otherwise}\,. \end{cases} \tag{24}$$

The first term on the RHS of Eq. (23) corresponds to edge-creation events between nodes i and j as before (see Sec. IV). The first part of the second term corresponds to gaining a network with adjacency matrix A_n from a network with adjacency matrix $A_{n,+}^{ij}$ by deleting an edge between i and j. Note that $\mathcal{D}$ is the rate of deletion per edge, so we multiply by the number of edges (which is equal to $(A_n)_{ij}+1$) between i and j. The second part of this term corresponds to losing a network with adjacency matrix A_n by deleting an edge between i and j (to produce a network with adjacency matrix $A_{n,-}^{ij}$).

The third term on the RHS of Eq. (23) corresponds to gaining a network with adjacency matrix

$$\begin{pmatrix} 0 & A_{12} & \dots & A_{1,i-1} & 0 & A_{1,i+1} & A_{1,i+2} & \dots & A_{1n} \\ 0 & 0 & \dots & A_{2,i-1} & 0 & A_{2,i+1} & A_{2,i+2} & \dots & A_{2n} \\ \vdots & & & & \vdots & & & & \vdots \\ 0 & 0 & 0 & \dots & 0 & A_{i-1,i+1} & A_{i-1,i+2} & \dots & A_{i-1,n} \\ 0 & 0 & 0 & \dots & 0 & 0 & 0 & \dots & 0 \\ 0 & 0 & 0 & \dots & 0 & 0 & A_{i+1,i+2} & \dots & A_{i+1,n} \\ 0 & 0 & 0 & \dots & 0 & 0 & \dots & 0 & A_{n-1,n} \\ 0 & 0 & 0 & \dots & 0 & 0 & \dots & 0 & 0 \end{pmatrix}$$

from an adjacency matrix

$$A_n^{i-} = \begin{pmatrix} 0 & A_{12} & \dots & A_{1,i-1} & A_{1,i+1} & A_{1,i+2} & \dots & A_{1n} \\ 0 & 0 & \dots & A_{2,i-1} & A_{2,i+1} & A_{2,i+2} & \dots & A_{2n} \\ \vdots & & & & & & & \vdots \\ 0 & 0 & 0 & \dots & A_{i-1,i+1} & A_{i-1,i+2} & \dots & A_{i-1,n} \\ 0 & 0 & 0 & \dots & 0 & A_{i+1,i+2} & \dots & A_{i+1,n} \\ 0 & 0 & 0 & \dots & 0 & \dots & 0 & A_{n-1,n} \\ 0 & 0 & 0 & \dots & 0 & \dots & 0 & 0 \end{pmatrix}$$

by relabeling nodes $j \to j+1$ for $j \geqslant i$ and adding a new unconnected node with label i (which we choose uniformly at random from the set $\{1,\dots,n\}$). The Kronecker delta δ ensures that this term is present only when $(A_n)_{ij} = (A_n)_{ji} = 0$. As in Sec. IV, the uniformly random choice of the label for the new node ensures that $\mathscr{F}_n^{A_n}(t,\vec{s}_n)$ is invariant with respect to index permutations.

We give the derivation of a reduced equation for $u_{k_1}(t,\boldsymbol{s}_1)$ in Appendix C. When we include edge deletion, we need an additional closure assumption in addition to the mean-field approximation (15); see Appendix C for details. Our low-dimensional

approximation to (23) is

$$\left[\frac{\partial}{\partial t}+\mathcal{L}^{(1)}\right]u_{k_1}(t,\boldsymbol{s}_1)=u_{k_1-1}(t,\boldsymbol{s}_1)\left[\int_{\mathbb{S}}\sum_{k_2=0}^{\infty}\mathcal{C}(\boldsymbol{s}_1,k_1-1,\boldsymbol{s}_2,k_2-1)u_{k_2-1}(t,\boldsymbol{s}_2)\,d\boldsymbol{s}_2\right]$$
$$-\,u_{k_1}(t,\boldsymbol{s}_1)\left[\int_{\mathbb{S}}\sum_{k_2=0}^{\infty}\mathcal{C}(\boldsymbol{s}_1,k_1,\boldsymbol{s}_2,k_2)u_{k_2}(t,\boldsymbol{s}_2)\,d\boldsymbol{s}_2\right]$$
$$+\frac{(k_1+1)u_{k_1+1}(t,\boldsymbol{s}_1)}{\int_{\mathbb{S}}\sum_{k_1=0}^{\infty}k_1u_{k_1}(t,\boldsymbol{s}_1)\,d\boldsymbol{s}_1}\left[\int_{\mathbb{S}}\sum_{k_2=0}^{\infty}\mathcal{D}(\boldsymbol{s}_1,k_1+1,\boldsymbol{s}_2,k_2+1)(k_2+1)u_{k_2+1}(t,\boldsymbol{s}_2)\,d\boldsymbol{s}_2\right]$$
$$-\frac{k_1u_{k_1}(t,\boldsymbol{s}_1)}{\int_{\mathbb{S}}\sum_{k_1=0}^{\infty}k_1u_{k_1}(t,\boldsymbol{s}_1)\,d\boldsymbol{s}_1}\left[\int_{\mathbb{S}}\sum_{k_2=0}^{\infty}\mathcal{D}(\boldsymbol{s}_1,k_1,\boldsymbol{s}_2,k_2)k_2u_{k_2}(t,\boldsymbol{s}_2)\,d\boldsymbol{s}_2\right]+\mathcal{J}\mathcal{P}(\boldsymbol{s}_1)\delta_{k_1,0}\,. \tag{25}$$

VI. NUMERICAL EXAMPLES

We now carry out Monte Carlo simulations of our stochastic network evolution process to illustrate the validity of Eqs. (19) and (25) for sufficiently large networks.

First, in Sec. VI A, we investigate numerically the validity of the mean-field assumption for our model when the state space is a point. Second, in Sec. VI B, we use an example scenario to demonstrate that a numerical solution of Eqs. (19) and (25) matches well with a full Monte Carlo simulation of the underlying process. Third, in Sec. VI C, we adapt the example scenario to consider the convergence of a network's degree distribution in the limit of large networks. Fourth, in Sec. VI D, we show that one can use our kinetic approximation as an alternative to some one-step network creation models proposed by Boguñá *et al.* [33]. Finally, in Sec. VI E, we briefly consider some further approximations that one can make to Eqs. (19) and (25).

A. Accuracy of our mean-field assumption

In the absence of a network structure, the validity of the mean-field approximation depends on the choice of $\mathcal{L}^{(n)}$, and it has been studied widely [37,38,49–51]. In the present paper, we focus on evolving network structure. In our exploration of the validity of the mean-field approximation in the network evolution model, we suppose that there is no state dependence in either the edge-creation rate $\mathcal{C}$ or the edge-deletion rate $\mathcal{D}$.

The two-particle degree distribution $P^{(2)}_{k_1,k_2}$ is the probability that two nodes selected uniformly at random without replacement have degrees k_1 and k_2. In our mean-field closure, we approximate this quantity by the product $P_{k_1}P_{k_2}$, where P_{k_1} is the probability that a single node selected uniformly at random has degree k_1 (and P_{k_2} is defined analogously). In Fig. 2, we compare the empirical distributions $P^{(2)}_{k_1,k_2}(t)$ and $P_{k_1}(t)P_{k_2}(t)$ generated from 100 realizations of Algorithm 1 using 125 particles (and no node creation).

We see that our mean-field approximation does well on this example, and the main error occurs when $k_1=k_2$, for which the product $P_{k_1}(t)P_{k_2}(t)$ of one-particle distributions is slightly larger than the two-particle distribution $P^{(2)}_{k_1,k_2}(t)$. This discrepancy arises because one cannot select the same node twice when evaluating the correlation function $P^{(2)}_{k_1,k_2}(t)$, so the probability of finding two nodes with the same degree is lower than that estimated by $P_{k_1}(t)P_{k_2}(t)$ (which corresponds to choosing two nodes uniformly randomly with replacement). The difference should therefore tend to 0 as $1/n$ as the number n of nodes becomes infinite.

One way to evaluate the difference between two probability distributions is the Kolmogorov–Smirnov (KS) test [52], which gives the probability ρ_{KS} that one rejects the hypothesis that the two distributions are equal. For $P^{(2)}_{k_1,k_2}(t)$ and $P_{k_1}(t)P_{k_2}(t)$, we find that $\rho_{\mathrm{KS}}\approx 2.0\times10^{-3}$.

B. Example scenario: Local state degree distribution

The example in Sec. VI A was particularly simple, as it focused only on the network aspect of the model. We now want to compare Monte Carlo simulations of a much more complicated evolving spatial network with a numerical solution of the reduced model (25). We select our new example to illustrate and evaluate all of the model components described in Table I. It does not represent any particular physical or biological process.

Let's consider noninteracting point particles in the unit square, so one can describe the state of each particle by its position vector $\boldsymbol{s}_i=(x_i,y_i)\in[0,1]^2$. We suppose that these positions evolve according to the SDEs [41]

$$dX_i=\mu\,dt+\sigma\,dW_t,\quad dY_i=\sigma\,dW_t, \tag{26}$$

where as before we use capital letters $\boldsymbol{S}_i=(X_i,Y_i)$ to distinguish random variables from the values that they take. We assume that the drift coefficient $\mu>0$ and volatility coefficient $\sigma>0$ are constant (corresponding to a constant diffusion coefficient $\sigma^2/2$). To initialize, we place 1000 particles with degree 0 uniformly at random in the rectangle $(X_i,Y_i)\in[0,1/10]\times[0,1]$. We impose reflective boundary conditions at $x=0$ and $x=1$, and we impose periodic boundary conditions at $y=0$ and $y=1$. To generate some spatial heterogeneity, we suppose that the rate of edge creation between nodes depends both on the distance between nodes and on the spatial coordinates of each node. We take

$$\mathcal{C}(\boldsymbol{S}_i,k_i,\boldsymbol{S}_j,k_j)=\left\{\begin{array}{ll}X_i+X_j, & \text{if } ||\boldsymbol{S}_i-\boldsymbol{S}_j||\leqslant\epsilon,\\ 0\,, & \text{otherwise}\end{array}\right\}. \tag{27}$$

In contrast, we suppose that the rate of edge deletion per edge between nodes i and j depends on the degrees of nodes i and

j but is independent of position. Specifically, we take

$$\mathcal{D}(\boldsymbol{S}_i,k_i,\boldsymbol{S}_j,k_j) = \frac{k_i+k_j}{10}. \tag{28}$$

We introduce new nodes of degree 0 at a rate $\mathcal{J}$ uniformly at random in the rectangle $(x,y) \in [0,1/10] \times [0,1]$. Therefore,

$$\mathcal{P}(x,y) = \begin{cases} 10, & \text{if } x < 1/10, \\ 0, & \text{otherwise}. \end{cases} \tag{29}$$

$$\begin{aligned} &\frac{\partial u_{k_1}}{\partial t}(t,x_1) + \mu \frac{\partial u_{k_1}}{\partial x_1}(t,x_1) - \frac{\sigma^2}{2}\frac{\partial^2 u_{k_1}}{\partial x_1^2}(t,x_1) \\ &\quad = \left[\sum_{k_2=0}^{\infty}\int_0^1 \hat{\mathcal{C}}(x_1,x_2)u_{k_2}(t,x_2)\,dx_2\right]\left[u_{k_1-1}(t,x_1) - u_{k_1}(t,x_1)\right] + \frac{(k_1+1)^2}{10}u_{k_1+1}(t,x_1) - \frac{k_1^2}{10}u_{k_1}(t,x_1) \\ &\qquad + \frac{\int_{\mathrm{S}}\sum_{k_2=1}^{\infty} k_2^2 u_{k_2}(t,\boldsymbol{s}_2)\,d\boldsymbol{s}_2}{\int_{\mathrm{S}}\sum_{k_2=1}^{\infty} k_2 u_{k_2}(t,\boldsymbol{s}_2)\,d\boldsymbol{s}_2}\left[\frac{k_1+1}{10}u_{k_1+1}(t,x_1) - \frac{k_1}{10}u_{k_1}(t,x_1)\right] + \mathcal{J}\mathcal{P}(x_1)\delta_{k_1,0}, \end{aligned} \tag{30}$$

where

$$\hat{\mathcal{C}}(x_1,x_2) = \begin{cases} 2(x_1+x_2)\sqrt{\epsilon^2 - |x_1-x_2|^2}, & \text{if } |x_1-x_2| \leqslant \epsilon, \\ 0, & \text{otherwise}. \end{cases} \tag{31}$$

We solve (30) with no-flux conditions at $x = 0$ and $x = 1$ and initial condition

$$u_{k_1}(t=0,x_1) = \begin{cases} 10^4\delta_{k,0}, & x_1 \in [0,1/10], \\ 0, & \text{otherwise}, \end{cases} \tag{32}$$

because initially there are 10^3 particles placed uniformly at random in $[0,1/10] \times [0,1]$.

In Fig. 4, we show a comparison between a Monte Carlo simulation of $u_k(t,x)$ using Algorithm 1 and a numerical solution of Eq. (30) using a second-order central difference finite-volume method (FVM) in space and a fourth-order Runge–Kutta scheme in time. We use the parameter values $\mu = 3/4$, $\sigma = 1/4$, $\mathcal{J} = 500$, and $\epsilon = 0.1$.

We observe that the distribution function $u_k(t,x_1)$ is nontrivial, and the reduced model does a good job of capturing the empirical distribution that we obtain from Monte Carlo simulations. The KS probability for the distributions in Fig. 4 is $\rho_{\mathrm{KS}} \approx 3.2 \times 10^{-2}$.

C. Limit of large networks

We expect our mean-field approximation to become more accurate as one considers larger networks. We now briefly investigate this hypothesis in the context of degree distributions. (Naturally, it is also relevant to consider this hypothesis for other quantities.)

For a network with n nodes, $u_k = O(n)$, so we see that Eq. (25) converges to a sensible limit as $n \to \infty$ if $\mathcal{C} = O(1/n)$ and $\mathcal{D} = O(1)$. To investigate the convergence for large n, we consider networks in which the number of nodes is constant in time (i.e., $\mathcal{J} \equiv 0$). We first consider networks in which there is no edge deletion (i.e., $\mathcal{D} \equiv 0$). We take the edge-creation rate to be $500/n$ times that given in Eq. (27). We choose all other parameters as in Sec. VI B.

In the top panel of Fig. 5, we show the mean degree distribution sampled over $10^6/n$ realizations of Algorithm 1 for $n = 125$, $n = 500$, $n = 2000$, and $n = 8000$. We also show the degree distribution calculated by solving the IPDE (30). Qualitatively, this figure supports the hypothesis that, at least for estimating the degree distribution, our mean-field approximation is more accurate for larger networks.

We now introduce edge deletion and choose $\mathcal{D}$ to be given by Eq. (28). We increase the rate of edge creation slightly by taking the edge-creation rate to be $750/n$ times that given in Eq. (27). We show the resulting mean degree distribution sampled over $10^6/n$ realizations of Algorithm 1 for $n = 125$, $n = 500$, $n = 2000$, and $n = 8000$ in the bottom panel of Fig. 5; we also show the degree distribution that we calculate by solving the IPDE (30).

D. One-step network creation versus kinetic approximations

Dynamic models of network creation can provide an alternative to one-step network creation. For example, in the $G(n,p)$ Erdős–Rényi (ER) model [1], one specifies that a network has n nodes and that each pair of nodes is connected with independent, homogeneous probability $p \in (0,1)$. (One can also consider $p = 0$ and $p = 1$, but these cases are uninteresting.) This leads to a binomial degree distribution $\mathrm{Bin}(n-1,p)$, which becomes the Poisson distribution $\mathrm{Pois}(np)$ in the limit $n \to \infty$ with fixed np. Reference [31] discussed an alternative, dynamic approach to an ER model in which an initially unconnected network has n nodes and each node connects to other nodes uniformly at random at a specified rate. In the $n \to \infty$ limit, one can solve a master equation to obtain a Poisson degree distribution, which coincides with the standard model when halted at a specific time (depending on the edge-creation rate). We also note work by Krioukov and Ostilli [53], who showed that certain equilibrium ensembles create the same distribution of graphs as nonequilibrium ensembles.

References [33,54] discussed a one-step network-creation model that allows nodes to have an associated state. Nodes

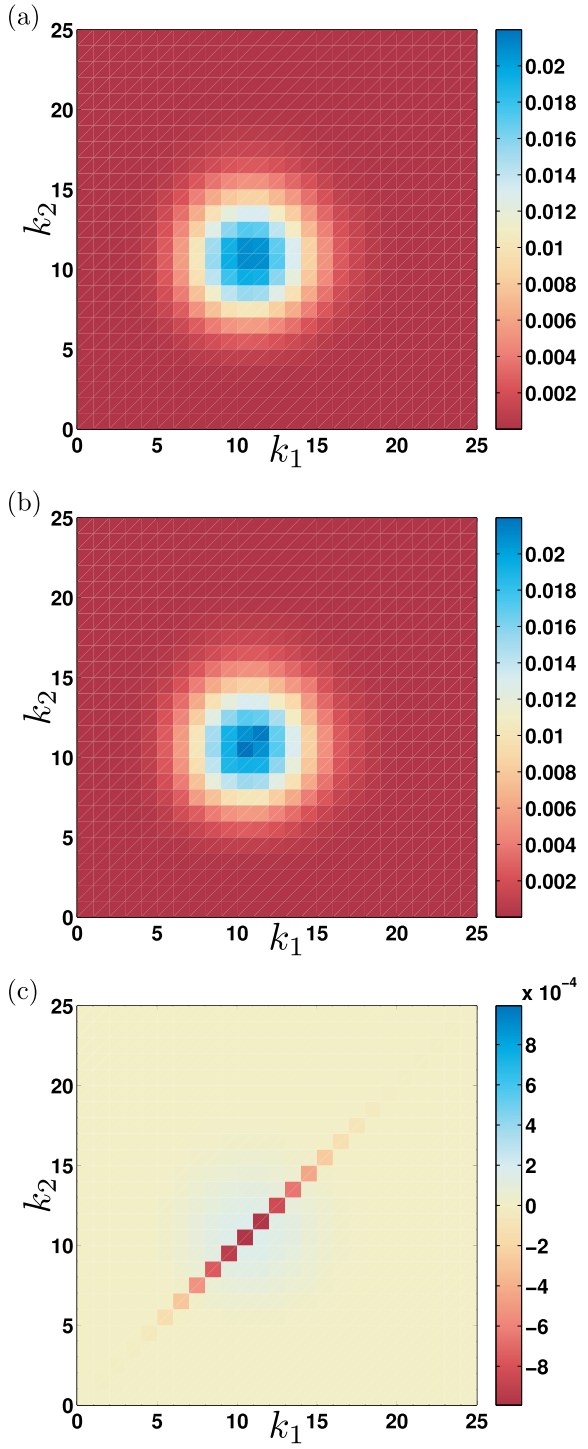

FIG. 2. Numerical illustration of the validity of the mean-field assumption (15). We average over 100 realizations of Algorithm 1 using $n = 125$ particles and a time step of $\Delta t = 10^{-3}$. No new particles enter the system ($\mathcal{J} = 0$), the edge-creation rate is $\mathcal{C}(k_i,k_j) = 2$, and the edge-deletion rate is $\mathcal{D}(k_i,k_j) = k_i + k_j$. We show (a) the two-particle distribution $P^{(2)}_{k_1,k_2}(t)$, (b) the product $P_{k_1}(t)P_{k_2}(t)$ of the one-particle distributions, and (c) the difference $P^{(2)}_{k_1,k_2}(t) - P_{k_1}(t)P_{k_2}(t)$ at time $t = 1/10$.

i and j have randomly distributed latent social variables $\boldsymbol{s}_i$ and $\boldsymbol{s}_j$, and these nodes are adjacent to each other with probability $r(\boldsymbol{s}_i,\boldsymbol{s}_j)$. References [33,54] then used a mean-field approximation to derive a formula for the degree distribution (depending on the probability distribution of the social variables and on the function r) of the network as the number of nodes tends to infinity.

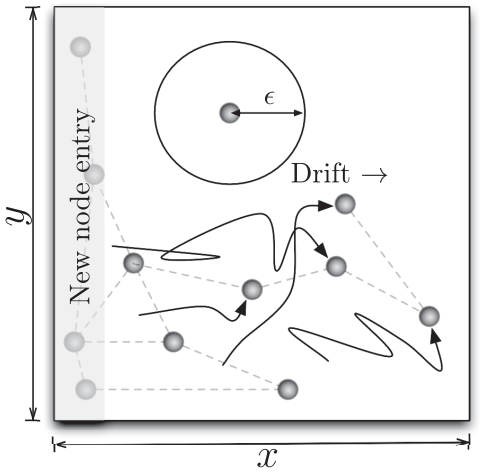

FIG. 3. Illustration of the example scenario in Sec. VI B. Nodes enter the system in a strip on the left-hand side of the unit square and then diffuse and drift to the right according to Eq. (26). There are reflective boundary conditions at $x = 0$ and $x = 1$ and periodic boundary conditions at $y = 0$ and $y = 1$. We create edges between nearby nodes according to Eq. (27). Edges are deleted at the rate given by Eq. (28).

One can use our kinetic approach as an alternative to one-step creation to examine such a scenario. To demonstrate this, we consider the case investigated in Ref. [33]. Suppose that the latent social variable is a positive scalar $\boldsymbol{s} = h \in [0,h_{\max}]$ and that

$$r(h_i,h_j) = \frac{1}{1 + (b^{-1}|h_i - h_j|)^{\alpha}} \tag{33}$$

for constants b and α. We solve Eq. (19) with an initial condition corresponding to n unconnected nodes that are distributed uniformly at random in a state space $[0,h_{\max}]$. No new nodes enter the system (i.e., $\mathcal{J} \equiv 0$), there is no edge deletion (i.e., $\mathcal{D} \equiv 0$), and the edge-creation rate is $\mathcal{C} = r(h_i,h_j)$. Thus, at time $T_{\text{end}} = 1$, the expected number of edges between node i and node j is $r(h_i,h_j)$. In Fig. 6, we see for parameter values $n = 1000$, $\alpha = 3$, and $b = 1/2$ that the degree distribution given by our mean-field model at $t = T_{\text{end}}$ matches very closely with the analytical formula of Ref. [33]. We solve the IPDE using a method of lines with a spatial discretization of $\Delta h = 1/4$ and a fourth-order Runge–Kutta scheme in time.

E. Final remarks: Moment closure

Despite the fact that Eqs. (19) and (25) are of much lower dimension than Eqs. (7) and (23), each of the former equations is still an infinite system of IPDEs, and they may still be too expensive to solve numerically. One can make further approximations by considering moments of the density $u_k(t,\boldsymbol{s})$ with respect to the degree k:

$$\mathcal{M}^{(r)}(t,\boldsymbol{s}) = \sum_{k=0}^{\infty} k^r u_k(t,\boldsymbol{s}). \tag{34}$$

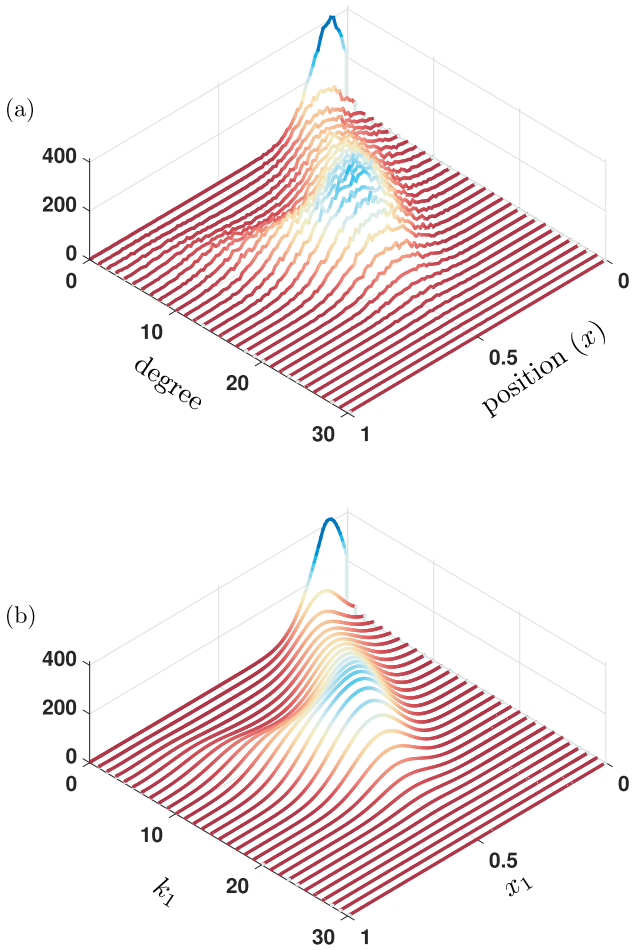

FIG. 4. Comparison of (a) the mean of 200 Monte Carlo simulations using Algorithm 1 binned into compartments of size $1/100$ along the x-axis and (b) $u_{k_1}(1/2,x_1)$ obtained from the numerical solution of Eq. (30). The parameter values are $\mathcal{J} = 500$, $\mu = 3/4$, $\sigma = 1/4$, and $\epsilon = 0.1$; and the time step in the stochastic (i.e., Monte Carlo) simulations is $\Delta t = 10^{-4}$. We initialize the simulations with 10^3 particles placed uniformly randomly in the domain $[0,1/10] \times [0,1]$. We show results at the final time $T_{\text{end}} = 1/2$.

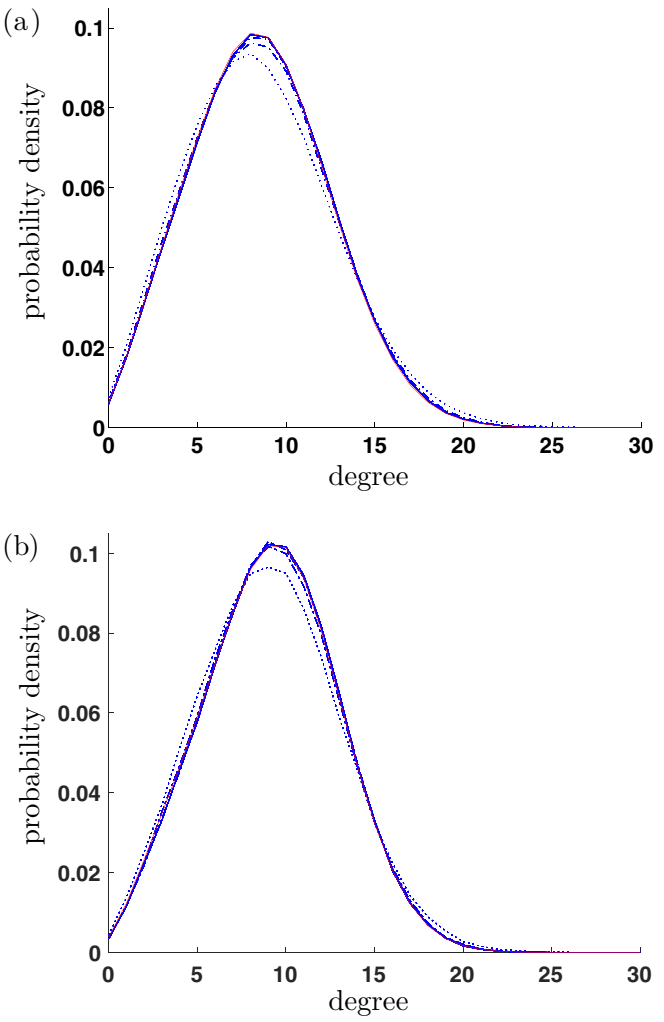

FIG. 5. Comparison of degree distribution at time $T_{\text{end}} = 1/2$ determined from Eq. (30) (red) and from a mean over multiple Monte Carlo simulations using Algorithm 1 with a time step of $\Delta t = 10^{-3}$ (blue). With n nodes (constant in time, so $\mathcal{J} \equiv 0$), we average the simulations are over $10^6/n$ realizations, where $n = 125$ (dotted curve), $n = 500$ (dash-dotted curve), $n = 2000$ (dash-dotted curve), and $n = 8000$ (solid curve). (a) No edge deletion (i.e., $\mathcal{D} \equiv 0$), and the edge-creation rate is $500/n$ times that given in Eq. (27). (b) The edge-deletion rate is given by Eq. (28), and the edge-creation rate is $750/n$ times that given in Eq. (27). The other parameter values are as in Sec. VI B.

In particular, $\mathcal{M}^{(0)}$ gives the number density of nodes (for which we obtain a closed equation if $\mathcal{J} \equiv 0$ and $\mathcal{L}^{(1)}$ does not depend on the network structure), and $\mathcal{M}^{(1)}$ gives the number density multiplied by the mean degree of a node with state vector $\boldsymbol{s}$. It is only possible to obtain a closed system of equations for particular choices of $\mathcal{C}$ and $\mathcal{D}$. In general, one needs to truncate the hierarchy of moment equations and then apply another closure assumption by positing an expression for a high-order moment in terms of lower-order moments [55–57].

VII. A MODEL FOR OSTEOCYTE NETWORK FORMATION

A. Osteocytes

An *osteocyte* [58] is a dendritic cell in both cortical bone (dense, weight-bearing bone) and trabecular bone (flexible, highly vascular bone). The protrusions (i.e., dendrites) of the cell are known as *processes*, and they form a communication network between the osteocytes and cells on the bone surface. To avoid confusion with the word "processes," which is common jargon in physics, we henceforth refer to *processes* as "dendrites." Osteocytes are densely packed in bone. They occupy spherical spaces called lacunae, and their dendrites occupy tunnels called canaliculi [59,60]. The dendrites enable communication via gap junctions, across which signaling molecules can diffuse. This communication network does not have a sole purpose, and many phenomena have been associated with it. It has been suggested that the exchange of signaling molecules relates to skeletal unloading, fatigue damage, and estrogen deficiency [61]. The range of signaling molecules that have been detected is vast, and many also arise in the regulation of other organs. These include Receptor

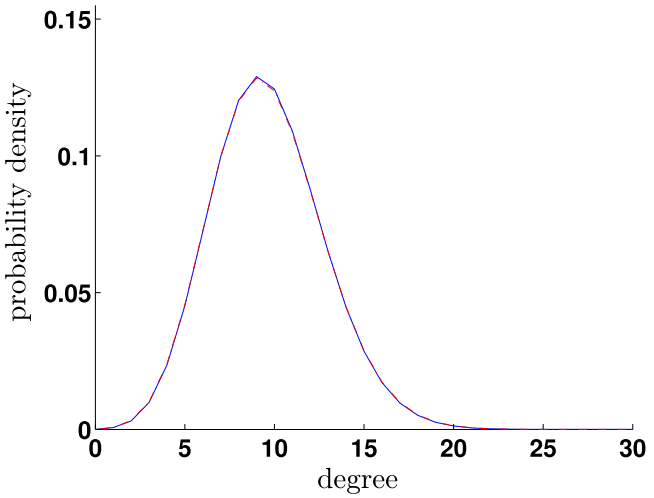

FIG. 6. Analytical approximation to the degree distribution (solid blue curve) of the latent social-space model given in Ref. [33] versus the result from a kinetic formulation (red dash-dotted curve) using Eq. (19). We uniformly distribute nodes with a social parameter $h \in [0,125]$. We use the parameter values $n = 1000$, $\alpha = 3$, and $b = 1/2$. The probability of connection and choice of $\mathcal{C}$ is given by Eq. (33). There is no edge deletion (i.e., $\mathcal{D} \equiv 0$), and the system is of constant size (i.e., $\mathcal{J} \equiv 0$). We solve the kinetic equation until a final time of $T_{\text{end}} = 1$.

Activator of Nuclear Factor Kappa-B Ligand (RANKL) [61], Vascular Endothelial Growth Factor (VEGF) [61], Parathyroid Hormone (PTH) [62], calcium ions (Ca^{2+}) [22], and Sclerostin [63]. Additionally, there is a thin layer of fluid around the osteocyte network. Perturbations to osteocyte-network organization can impact both fluid flow and diffusion, and they thereby allow mechanosensation and signaling [64].

Because of the location of osteocyte networks in bone, it is difficult to examine them experimentally. In Fig. 7, we show the outcome of applying an obtrusive experimental technique to view osteocytes after nearby mineral has been dissolved. Three-dimensional imaging data is now available by using confocal microscopy [65–67], and such work has led to the identification of some structural features of osteocyte networks. Identified features include the mean number of dendrites that protrude from each osteocyte [67] and mean lengths of a canicular network [68]. Other work has reported that high-density networks correlate positively with high bone quality. Note that the mineral matrix has an orientation (from dendrites and collagen), and bone quality is associated with the level of organization of this mineral matrix [64].

FIG. 7. Scanning electron micrograph of osteocytes in bone. The sample was prepared by embedding the bone in resin, which was subsequently etched with perchloric acid. The image was created by removing the entire mineral in the sample, leaving a replica of the cells. Therefore, what is observed is the resin that filled the spaces in the bone and the spaces inside the cells. (This picture is copyrighted work and is available via Ref. [69] from Ref. [70].)

B. Formation process

On the bone-tissue interface, two cell types are actively involved in the bone-formation process: *osteoblasts* and *osteoclasts*. Osteoblasts form a layer on the bone surface and secrete the osteoid bone matrix. The larger multinucleated osteoclasts subsequently resorb the bone matrix [71]. Osteoblasts also express RANKL and osteoprotegerin (OPG). The former promotes bone resorption by osteoclasts, and the latter inhibits it. This is one example for how osteoblasts tightly regulate bone formation and destruction. As the osteoblasts produce the calcium matrix, occasionally they become embedded within the bone. These osteoblasts then change morphology to become star-shaped osteocytes.

Osteoblasts originate from mesenchymal cells and have one of four possible fates: undergo apoptosis (approximately 65%), become embedded in bone as osteocytes (approximately 30%), transform into inactive osteoblasts and become bone-lining cells, or transdifferentiate into cells that deposit chondroid bone [21]. Upon some signaling event, osteoclasts arrive at a bone and the osteoblasts move aside. The osteoclasts then burrow into the bone; as they do this, they resorb some of the osteocyte matrix. It has been suggested that after an osteocyte undergoes apoptosis, pro-osteoclastogenic signals are released by the osteocyte's neighbors in the network [72]. A trail of osteoblasts then follows the osteoclasts and secretes new bone matrix [73], although some of these get left behind to become osteocytes. Kamioka *et al.* suggested that osteoblasts are incorporated into a network by osteocytes extending their dendrites towards the osteoblast layer [65].

Thus far, we have discussed three types of bone cells: osteoblasts, osteoclasts, and osteocytes. For at least the osteoblast-to-osteocyte cell transition, biologists have subdivided the process of cell differentiation to include eight phenotypes: (1) preosteoblast, (2) preosteoblastic osteoblast, (3) osteoblast, (4) osteoblastic osteocyte, (5) osteoid-osteocyte (i.e., Type-II preosteocyte), (6) Type-III preosteocyte, (7) young osteocyte, and (8) old osteocyte [21]. Additionally, the secretion of bone occurs as two steps: first, osteoid is laid as a scaffold, moving the interface (the *deposition front*) between premature bone and tissue; and then mineralization occurs (at the *mineralization front*) to confer strength. Stages (4)–(6) are cells between the deposition and mineralization fronts; they are surrounded by a non-mineralized osteoid matrix. (In other words, there is a scaffold around them.) Stages (7)–(8) are cells whose volume has depleted (by reduction in the endoplasmic reticulum and Golgi apparatus)

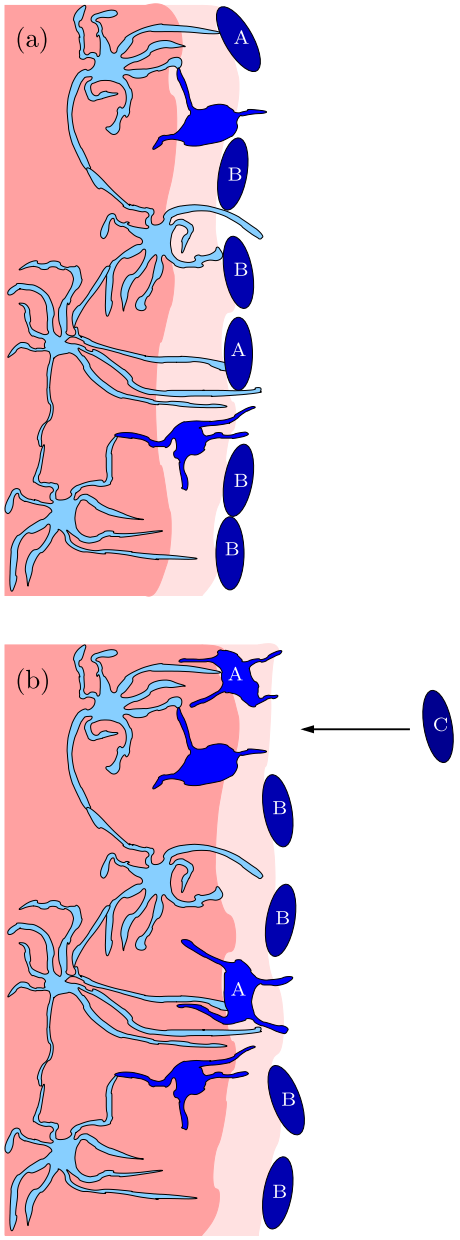

FIG. 8. Diagrammatic illustration of the bone-formation process. Lighter shades of blue indicate more differentiated cells. The lighter shade of pink indicates the deposition front, and the darker shade of pink indicates the mineralization front. Panel (a) occurs earlier than panel (b). Dendritic osteocytes (light blue) have dendrites that extend towards the osteoblast layer (dark blue). The osteoblasts secrete bone matrix. Osteoblast cells marked with "A" are signaled by the osteocyte network to differentiate into osteocytes. Osteoblast cells marked with "B" do not differentiate and stay on the outer bone surface. Osteoblast cells marked with "C" arrive at the deposition front after differentiating from precursor osteoblasts (pre-osteoblasts). (This figure is inspired by a similar illustration in Ref. [21].)

and are in mineralized bone. The diagram in Fig. 8 shows the bone-formation step. Although it is potentially useful to consider all of the above phases (defined from osteogenic markers), we are interested only in the structure of a mature osteocyte network [stages (6)–(8)], so we will make drastic simplifications.

1. Bone metastasis

Advanced prostate, breast, and lung cancer can metastasize to bone [74,75]. In pathological bone, the highly regulated bone-remodeling signaling pathway is disrupted. A particularly painful symptom is net bone formation in some regions and simultaneous weakening in other areas [76]. Small bone lesions can also develop.

In a cancerous microenvironment, transforming growth factor-beta (TGF-β) expressed by tumor cells promotes excessive osteoblast growth [77]. The overexpression of TGF-β is only one of the many ways in which tumors can interfere with bone formation; TGF-β targeted cancer therapy has been only marginally successful [78].

Ordinary differential equation (ODE), and hence non-spatial, models for cell populations in healthy bone that incorporate osteoblast, osteoclast, and osteocyte populations were developed in Refs. [79–81]. Partial differential equation (PDE) models of healthy bone remodeling include [82,83], and these models were adapted subsequently for cancerous bone in Ref. [84]. Mechanically-focused models that capture stresses and strains in bone have also been explored [76,85,86]. A few of these models consider osteocyte density, but none of them explore network structure.

A seemingly unexplored area is the investigation of osteocyte network morphology in the presence of cancer. There is evidence in Refs. [87,88] that for myeloma and (benign) osteoma, osteocytes are exceptionally spherical and have shorter, distorted dendrites that are also reduced in number in comparison to healthy tissue. A contrasting osteocyte network with unregulated excessive dendritic growth (and hence a larger numbers of dendrites) was observed in the presence of osteogenic sarcoma [87].

In Sec. VII C, we develop a simple model that incorporates network properties into the bone-formation process. For some cancer types, it is known in part how bone formation is affected (e.g., there is increased osteoblast proliferation). Using such a model, it may be possible to connect a change in the bone-formation process to the properties of the resulting osteocyte network. Qualitatively, one would then be able to suggest which osteocyte network phenotype is promoted by a particular cancer (e.g., stunted dendrite growth, excessive dendrite growth, etc.). Conversely, it may be possible to infer changes in the bone-formation process from observations of osteocyte network structure.

C. Model of osteocyte network growth

The model that we develop in this section builds on the work of Buenzli [19]. We avoid modeling the full complications of the biology (e.g., cell subclassifications, proteins, etc.) and consider only osteoblasts and osteocytes. By examining a simple model, we hope to gain insight into how osteocyte network structure may depend on measurable quantities, while preserving a minimalist approach.

The osteocyte network occupies an expanding domain $\Omega(t) \subset \mathbb{R}^d$ with a boundary $\partial\Omega(t)$ that moves with normal velocity $v(t)$. The nodes in the network are osteocytes, which each have an associated position in $\mathbb{R}^d$. The undirected edges are the dendrites between them. We allow multiedges, which correspond to multiple dendritic connections between the same

pair of osteocytes, and they are observed in practice [64]. We suppose that the positions of the osteocytes are time-independent, so $\mathcal{L}^{(1)} \equiv 0$.

Motivated by the observation that osteoblasts differentiate to osteocytes near the deposition front [21], where there is less mineralization, we suppose that the rate at which an osteocyte creates connections to other osteocytes is governed by the local bone mineral density $m(t,\boldsymbol{x}) \in \mathbb{R}^+$.

Our model consists of two processes: (1) domain expansion and (2) edge creation within semimineralized bone. Buenzli's model [19] consists entirely of domain expansion, whereas we also incorporate network structure.

1. Domain expansion

We suppose that osteoblasts are encased within the mineral matrix and become osteocytes with degree $k = 0$ at a rate of $D_{\text{burial}}(t,\boldsymbol{x})\rho_{\text{Ob}}(t,\boldsymbol{x})$ for $\boldsymbol{x} \in \partial\Omega(t)$, where $D_{\text{burial}}(t,\boldsymbol{x})$ is the probability per unit time of an osteoblast joining the matrix and $\rho_{\text{Ob}}(t,\boldsymbol{x})$ is the surface density of osteoblasts. [We take $\rho_{\text{Ob}}(t,\boldsymbol{x})$ to be given.] Equation (19) is then

$$\mathcal{JP}(t,\boldsymbol{x}) = D_{\text{burial}}(t,\boldsymbol{x})\rho_{\text{Ob}}(t,\boldsymbol{x})\delta_{\partial\Omega(t)}(\boldsymbol{x}), \tag{35}$$

where

$$\delta_{\partial\Omega(t)}(\boldsymbol{x}) = \int_{\partial\Omega(t)} \delta(\boldsymbol{x}-\boldsymbol{x}')\,dS'.$$

Following Ref. [19], we suppose that the (outward) normal velocity of the interface is

$$v(t,\boldsymbol{x}) = \kappa_{\text{form}}(t,\boldsymbol{x})\rho_{\text{Ob}}(t,\boldsymbol{x}), \quad \boldsymbol{x} \in \partial\Omega(t), \tag{36}$$

where $\kappa_{\text{form}}(t,\boldsymbol{x})$ is the volumetric rate at which osteoblasts form the mineral matrix.

2. Edge creation in semimineralized bone

We suppose that the mineral density $m(t,\boldsymbol{x})$ of the matrix can vary in both space and time, as mineral is produced by both osteoblasts at the deposition front and osteocytes behind it. We suppose that there is a maximum mineral density C_m that corresponds to fully mineralized bone, that osteocytes produce mineral at a rate of $r_{\text{exc}}^{(\text{Cy})}(1-m/C_m)$ per cell, and that osteoblasts produce mineral at a rate of $r_{\text{exc}}^{(\text{Ob})}$ per cell, where $r_{\text{exc}}^{(\text{Cy})}$ and $r_{\text{exc}}^{(\text{Ob})}$ are constants. Therefore,

$$\frac{\partial}{\partial t}m(t,\boldsymbol{x}) = r_{\text{exc}}^{(\text{Cy})} f(t,\boldsymbol{x})\left[1-\frac{m(t,\boldsymbol{x})}{C_m}\right] + r_{\text{exc}}^{(\text{Ob})}\rho_{\text{Ob}}(t,\boldsymbol{x})\delta_{\partial\Omega(t)}(\boldsymbol{x}), \tag{37}$$

where $f(t,\boldsymbol{x})$ [given by Eq. (1)] is the density of osteocytes. Note that κ_{form} is the volume of matrix produced per osteoblast per unit time, whereas $r_{\text{exc}}^{(\text{Ob})}$ is the mass of matrix produced per osteoblast per unit time, so the density of matrix formed by the osteoblasts is $r_{\text{exc}}^{(\text{Ob})}/\kappa_{\text{form}}$, which should be no larger than the maximum mineral density C_m. Note additionally that because D_{burial} is the rate at which osteoblasts join the matrix and κ_{form} is the rate at which matrix volume is produced, the ratio $D_{\text{burial}}/\kappa_{\text{form}}$ is the density of newly formed osteocytes.

We now model how edges (i.e., dendrites) form. We suppose that the rate of edge creation depends on the mineral density m. In Ref. [65], it was suggested that osteocytes grow dendrites towards the osteoblast layer. This suggests that dendrites grow in the part of the domain that is not fully mineralized. To construct a simple model in which edges are less likely to form as mineral density becomes larger, we let the rate of edge creation between nodes at positions $\boldsymbol{x}$ and $\boldsymbol{y}$ be

$$\mathcal{C}(t,\boldsymbol{x},\boldsymbol{y}) = [C_m - m(t,\boldsymbol{x})][C_m - m(t,\boldsymbol{y})]g(||\boldsymbol{x}-\boldsymbol{y}||), \tag{38}$$

where g is monotonically decreasing and vanishes at infinity, encoding the fact that short edges are much more likely to form than long edges. Equation (38) takes into account the mineral density only at the two endpoints $\boldsymbol{x}$ and $\boldsymbol{y}$. One can formulate more complicated models in which $\mathcal{C}$ depends on (for example) a line integral of m between $\boldsymbol{x}$ and $\boldsymbol{y}$. However, given the simplifications and modeling assumptions that we have already made, we do not consider such complicated edge-creation models.

With our model assumptions, Eq. (19) becomes

$$\frac{\partial}{\partial t}u_k(t,\boldsymbol{x}) = \left[\int_{\Omega(t)} \mathcal{C}(t,\boldsymbol{x},\boldsymbol{y})f(t,\boldsymbol{y})\,d\boldsymbol{y}\right][u_{k-1}(t,\boldsymbol{x}) - u_k(t,\boldsymbol{x})] + D_{\text{burial}}(t,\boldsymbol{x})\rho_{\text{Ob}}(t,\boldsymbol{x})\delta_{\partial\Omega(t)}(\boldsymbol{x})\delta_{k,0}. \tag{39}$$

Equation (39) is coupled through $\mathcal{C}$ to Eq. (37) for the mineral density, and the domain $\Omega(t)$ evolves according to Eq. (36).

Summing (39) over k yields

$$\frac{\partial f(t,\boldsymbol{x})}{\partial t} = D_{\text{burial}}(t,\boldsymbol{x})\rho_{\text{Ob}}(t,\boldsymbol{x})\delta_{B(t)}(\boldsymbol{x}), \tag{40}$$

which is identical to Eq. (8) in Ref. [19]. Note also that Eq. (39) does not include feedback between network structure and the burial rate D_{burial}, though one can extend the model to incorporate such coupling.

D. Traveling-wave solution

If D_{burial}, κ_{form}, and ρ_{Ob} are constant, then Eqs. (36), (37), and (39) admit a traveling-wave solution that corresponds to the sustained creation of new bone. Such a solution may give an indication of the local behavior near growing bone, and we can use it to determine how the properties of the bone depend on the parameters in the model.

For a one-dimensional traveling wave that moves with a constant speed of $v = \kappa_{\text{form}}\rho_{\text{Ob}}$, we can (without loss of generality) take the domain to be $\Omega(t) = (-\infty, vt)$. We transform to coordinates that move with the wave by writing $z = x - vt$, and we seek a solution in which u_k and m depend only on z. Equation (39) becomes

$$-v\frac{d}{dz}u_k(z) = D_{\text{burial}}\rho_{\text{Ob}}\delta(z)\delta_{k,0} + \left[\int_{-\infty}^{0} \mathcal{C}(z,z')f(z')\,dz'\right][u_{k-1}(z) - u_k(z)]. \tag{41}$$

Summing over k gives

$$-v\frac{d}{dz}f(z) = D_{\text{burial}}\rho_{\text{Ob}}\delta(z),$$

so

$$f(z) = \frac{D_{\text{burial}}}{\kappa_{\text{form}}}[1 - H(z)], \tag{42}$$

where $H(x)$ is the Heaviside function. Equation (42) is identical to Eq. (13) in Ref. [19] when D_{burial} and κ_{form} are constant. Using (42) in Eq. (41) gives

$$\frac{d}{dz}u_k(z) = -b\delta(z)\delta_{k,0} - a(z)[u_{k-1}(z) - u_k(z)]\,, \qquad (43)$$

where

$$b = \frac{D_{\text{burial}}}{\kappa_{\text{form}}}\,, \quad a(z) = \frac{D_{\text{burial}}}{\kappa_{\text{form}}^2\rho_{\text{Ob}}}\int_{-\infty}^{0}\mathcal{C}(z,z')\,dz'.$$

Equivalently, one can write Eq. (43) as

$$\frac{d}{dz}u_k(z) = -a(z)[u_{k-1}(z) - u_k(z)]\,, \quad u_k(0) = b\,\delta_{k,0}\,, \qquad (44)$$

whose solution is

$$u_k(z) = \frac{b\lambda^k e^{-\lambda}}{k!}\,, \quad \lambda = \int_z^0 a(z')\,dz'. \qquad (45)$$

The density of newly formed osteocytes b sets the scale for u_k.

Before we can solve for λ (which is equal to the mean degree), we first need to solve for $m(z)$. Solving Eq. (37) yields

$$m(z) = C_m + \left(\frac{r_{\text{exc}}^{(\text{Ob})}}{\kappa_{\text{form}}} - C_m\right)\exp\left(\frac{r_{\text{exc}}^{(\text{Cy})}D_{\text{burial}}z}{\kappa_{\text{form}}^2\rho_{\text{Ob}}C_m}\right). \qquad (46)$$

We see that the mineral density varies from that produced by osteoblasts $r_{\text{exc}}^{(\text{Ob})}/\kappa_{\text{form}}$ to the maximum mineralization C_m over a length scale of

$$L = \frac{\kappa_{\text{form}}^2\rho_{\text{Ob}}C_m}{r_{\text{exc}}^{(\text{Cy})}D_{\text{burial}}}\,.$$

We illustrate this behavior in Fig. 9(a).

Before we can evaluate λ, we need to choose a form for g. Suppose first that g is a constant, and let's write $g \equiv \beta$. In principle, this may allow long edges to form—recall [see Eq. (38)] that we argued that g should decay at infinity to ensure a low probability for long edges to form—but we see from Eq. (46) that even with g identically constant, $C(z,z')$ approaches 0 exponentially fast over the length scale L, which therefore sets the scale for the maximum edge length.

Inserting Eq. (46) in Eq. (45) gives $\lambda = \lambda_\infty(1 - e^{z/L})$, where

$$\lambda_\infty = \frac{\beta\rho_{\text{Ob}}C_m^2\kappa_{\text{form}}^2}{D_{\text{burial}}(r_{\text{exc}}^{(\text{Cy})})^2}\left(C_m - \frac{r_{\text{exc}}^{(\text{Ob})}}{\kappa_{\text{form}}}\right)^2, \qquad (47)$$

which indicates that the mean degree varies over the same length scale from a value of 0 for newly formed osteocytes to a value of λ_∞ deep within a bone.

In Fig. 9(b), we illustrate the traveling-wave profile of the degree distribution by plotting $(1/b)\sum_{k=0}^{K}u_k(z)$ for several values of K. The differences between these curves indicate the proportion of osteocytes of each degree. As expected, there is a region at the front of the wave in which the mean degree of the osteocytes is reduced, and the LSDD approaches a stationary distribution far behind the front.

If, instead of taking g to be constant, we instead choose $g(z,z') = \beta e^{-|z-z'|/l}$ or $g(z,z') = \beta e^{-|z-z'|^2/l^2}$, we obtain qualitatively similar results, provided $l > L$. For example, in the first case,

$$\lambda = \lambda_\infty\frac{l(l - le^{z/L+z/l} - L + Le^{2z/L})}{l^2 - L^2}\,.$$

For $l \gg L$, we see that $\lambda \to \lambda_\infty(1 - e^{z/L})$. For $l \ll L$, we see that $\lambda \to \lambda_\infty(l/L)(1 - e^{2z/L})$, so the length scale over which degree varies is halved and the mean degree is smaller by a factor of l/L.

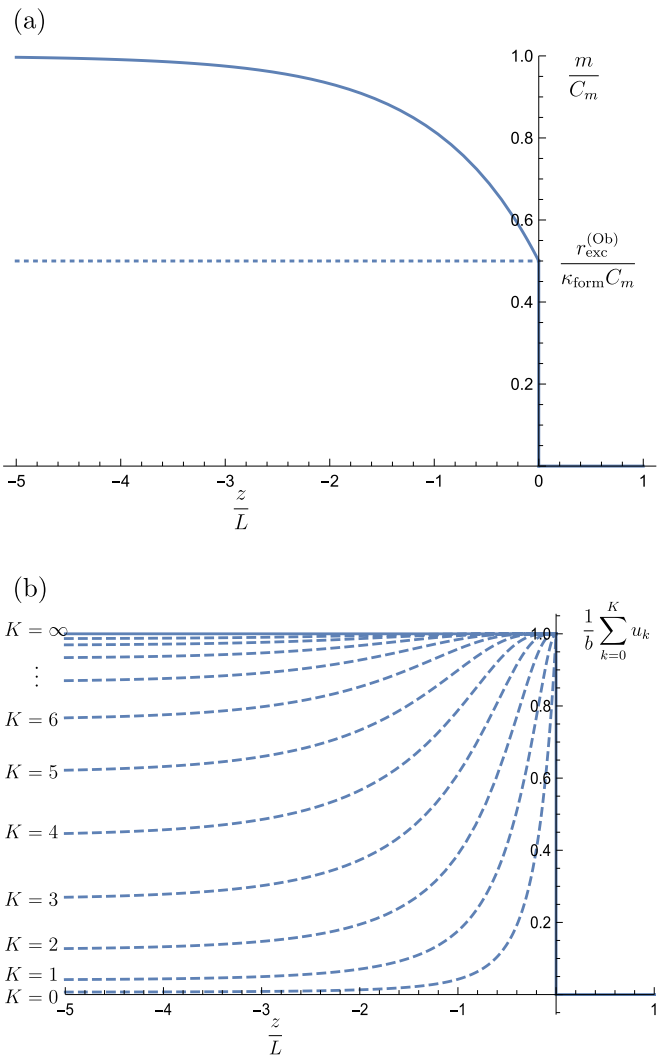

FIG. 9. (a) Traveling-wave profile of mineral density m normalized by C_m. At the front of the wave, $m = r_{\text{exc}}^{(\text{Ob})}/\kappa_{\text{form}}$ (dashed line), which we choose to be $0.5C_m$ in the figure. Behind the front, m approaches C_m. (b) The solid curve is a traveling-wave profile of osteocyte density $f = \sum_{k=0}^{\infty}u_k$, normalized by $b = D_{\text{burial}}/\kappa_{\text{form}}$. We illustrate the degree distribution of osteocytes as a function of position by showing $\sum_{k=0}^{K}u_k$ (dashed curves) for the case $\lambda_\infty = 5$. The lower ($K = 0$) curve illustrates the proportion of osteocytes with degree 0, and the difference between the $K = i$ and $K = i - 1$ curves illustrates the proportion of osteocytes with degree i.

E. Parametrization and interpretation

One can infer representative values of some of the parameters and variables in our model from existing experimental data. For example, in the review paper [68], the authors

calculated the number of osteocytes per mm^3 to lie in the range 19000–28500 mm^{-3}; the surface density ρ_{Ob} of osteoblasts per mm^2 was calculated in Ref. [89] (using data from Ref. [90]) to be in the range 2000–10000 mm^{-2}; and values of D_{burial} and κ_{form} were given in Ref. [19] (using data from Refs. [90,91]) for bone near a Haversian canal (which occurs only in cortical bone). The number of dendrites that protrude from an osteocyte yielded a mean degree of about 52.7 in Ref. [67]. As suggested in Refs. [64–66], we expect the number of unique neighbors of an osteocyte to be smaller by an order of magnitude. Measurements of the speed of the deposition front of bone creation were given in Ref. [92]. Numerous other parameters (e.g., the rate $r_{exc}^{(Cy)}$ at which osteocytes produce mineral and the maximum mineral density C_m) are unknown, and the values above were reported in only a few papers, so it is not yet possible to make quantitative predictions with our model.

Despite the dearth of knowledge about parameter values, we can use our model to make qualitative predictions of the effect of varying each parameter. The review [93] summarizes how different cancer types interfere with healthy bone remodeling. In particular, the review details how factors produced by prostate cancer cells lead to net bone formation due to increased levels of proliferation and differentiation of osteoblasts. In our model, an increased level of differentiation corresponds to an increased burial rate D_{burial}. Increasing D_{burial} in the model increases the number density of osteocytes f, but it decreases the mean degree λ. In other words, it decreases the mean number of dendrites that leave a cell body. In the model, this occurs because an increase in osteocyte density leads to an increase in mineralization, which makes dendrite formation less likely.

It was shown in Refs. [87,88] that for myeloma and benign osteoma—two other cancers that can cause net bone formation [94]—osteocytes are rather spherical, with shorter, distorted dendrites that are fewer in number in comparison to those in healthy tissue. Although these articles do not comment on osteocytes density or on mineralization, and it is crucial to be careful to avoid over-interpreting such limited data, our model does suggest one possible mechanism for this change in morphology.

VIII. CONCLUSIONS

We introduced a model for evolving spatial networks, and we used a mean-field approximation to reduce the dimension of its governing hierarchal Fokker–Planck equations. Specifically, by defining a local state degree distribution, we derived IPDEs (19) and (25) to describe an evolving spatial network that includes evolution of the position of nodes (or some more general state vector), edge creation, edge deletion, and node creation that occur at prescribed rates. Our approach generalizes commonly studied master-equation approaches by including a state space so that we can examine spatial networks.

To illustrate the potential utility of our IPDEs in applications, we examined growing osteocyte networks in bone. Although we employed a very simplistic model, we were able to use it predict relationships between biological parameters and network structure. Our approach provides a starting point for examining spatial networks in biology and other fields. In the future, we hope to compare predictions to experimental data after making a model more faithful to the biology.

There are also various ways to generalize our approach, and we briefly indicate two of them. First, in all of our examples, the motion in state space is independent of network structure. There are many scenarios in which motion should depend on the network, and one can readily extend our mean-field approach to situations in which the motion of a node depends on its degree (and even on the degrees of its neighbors). For example, for pairwise interactions, it is straightforward to extend our model to the case in which the interaction depends on the degrees of the two nodes as well on as their positions. However, network information (e.g., a local clustering coefficient) that is not expressible in terms of node degrees requires the incorporation of extra closure assumptions. Second, in our model of network evolution, nodes are created or removed according to Poisson processes, so our model can generate multiedges. One can extend our approach to simple graphs, in which multiedges are not allowed, with an additional closure assumption. In the edge-creation term, the creation of an edge should be abandoned if an edge already exists between a pair of nodes. One then multiplies the term $\mathcal{C}(\boldsymbol{s}_i,k_i,\boldsymbol{s}_j,k_j)$ by the probability that there is no existing edge between nodes i and j. This probability is approximately $1-k_ik_j/(2m)$, where k_i and k_j are the node degrees and m is the total number of edges.

ACKNOWLEDGMENTS

J.P.T.-K. received funding from the EPSRC under Grant No. EP/G037280/1, and D.B. acknowledges funding from the National Cancer Institute (U01 CA202958-01). We thank Marc Barthelemy, Pascal Buenzli, Richard Janis Goldschmidt, Mikko Kivelä, Andrew Krause, Conor Lynch, Joel Miller, Se Wook Oh, Jan Poleszczuk, and particularly Paul Dellar for helpful discussions.

APPENDIX A: CANDIDATE ALGORITHM FOR THE KINETIC NETWORK MODEL

In Algorithm 1, we give pseudocode for our simulations of evolving spatial networks. In the main text, we summarized our model in Table I.

When simulating Algorithm 1, we use a small time step Δt, so $0 < \Delta t \ll 1$. We also specify the following ordering of events: edge creation; edge deletion; state update; and then new particles are allowed to enter the system. This specification is arbitrary, and obviously it is desirable that any reordering of these events becomes inconsequential as $\Delta t \to 0$. For our numerical experimentation using the examples in Sec. VI, this indeed appears to be the case. For the simulations that we reported in Sec. VI, we chose a time step Δt to be sufficiently small that a reordering of events has no discernible impact.

The update rule for event (d) in Table I—namely, the evolution of the states of the individual nodes—depends on the particular process that we consider. We write $\boldsymbol{s}_i(t+\Delta t) = \mathscr{D}(\boldsymbol{s}_1(t),\ldots,\boldsymbol{s}_{N(t)}(t),\Delta t)$, where $\mathscr{D}$ arises from the time discretization of the underlying process. For example, one can use an Euler–Maruyama method or the Milstein method for the SDE (4) [95]; and one use Störmer–Verlet schemes for the ODEs in Eq. (3).

Algorithm 1: Algorithm to generate an evolving spatial network. The notation $\mathsf{randperm}(X)$ signifies a permutation, selected uniformly at random, of the discrete set X.

Data: Choose an end time $T_{\text{end}} = M\Delta t$ for large $M \in \mathbb{N}$ and small $\Delta t > 0$.
Set the number of particles $N \leftarrow N_0$.
Initialize the starting state at $\boldsymbol{s}_i \leftarrow \boldsymbol{s}_0^{(i)}$ and starting degree at $k_i \leftarrow k_0^{(i)}$ for each $i \in \{1, \ldots, N_0\}$.
Set time counter $m \leftarrow 0$.
while $m \leq M$ **do**

%Edge-creation update.

for $i \leftarrow \mathsf{randperm}(\{1, 2, \ldots, N\})$ **do**

for $j \leftarrow \mathsf{randperm}(\{i+1, \ldots, N\})$ **do**

Draw a uniform random number r_1 from the distribution $\mathcal{U}(0, 1)$.

if $r_1 \leq \mathcal{C}(\boldsymbol{s}_j, k_j | \boldsymbol{s}_i, k_i)\Delta t$ **then**

Create an edge between node i and node j.

%Edge-deletion update.

for $i \leftarrow \mathsf{randperm}(\{1, 2, \ldots, N\})$ **do**

for $j \leftarrow \mathsf{randperm}(E_i)$ **do** *%E_i is the set of nodes joined by an edge to i, counted according to multiplicity.*

Draw a uniform random number r_2 from the distribution $\mathcal{U}(0, 1)$.

if $r_2 \leq \mathcal{D}(\boldsymbol{s}_j, k_j | \boldsymbol{s}_i, k_i)\Delta t$ **then**

Delete an edge between node i and node j.

%State update.

for $i \leftarrow 1$ **to** N **do**

Update particle state: $\boldsymbol{s}_i \leftarrow \mathscr{D}(\boldsymbol{s}_1, \ldots, \boldsymbol{s}_N, \Delta t)$. *%$\mathscr{D}$ arises from the time-discretization of the state dynamics*

%Node creation.

Draw a uniform random number r_3 from the distribution $\mathcal{U}(0, 1)$.

if $r_3 \leq \mathcal{J}\Delta t$ **then**

Create node with state $\boldsymbol{s}_{N+1} \leftarrow \boldsymbol{s}^*$, where $\boldsymbol{s}^* \sim \mathcal{P}$.

Initialize the degree $k_{N+1} \leftarrow 0$

Update the number of particles: $N \leftarrow N + 1$.

Update time: $m \leftarrow m + 1$.

One can devise an efficient simulation algorithm for situations in which edge creation or deletion do not depend on the state of nodes. In that case, one can use an event-driven algorithm, such as a Gillespie algorithm [96], for creation and deletion events.

APPENDIX B: ADDITIONAL DETAILS OF THE MODEL DERIVATION: NO EDGE DELETION

In this appendix, we fill in the details of the derivation in Sec. IV B. When we sum over the degrees and integrate over the states of particles 2 through n, multiply by n, and sum over n, the first term on the RHS of Eq. (7) gives

$$\sum_{n=0}^{\infty} n \sum_{\vec{k}_n \in K_{2,n}} \int_{\mathbb{S}^{n-1}} \sum_{i=1}^{n} \sum_{j=i+1}^{n} \mathcal{C}(\boldsymbol{s}_i, k_i - 1, \boldsymbol{s}_j, k_j - 1) \mathcal{F}_n^{\vec{k}_{n,-}^{ij}}(t, \vec{s}_n)\, d\vec{s}_n^{(2)} - \sum_{n=0}^{\infty} n \sum_{\vec{k}_n \in K_{2,n}} \int_{\mathbb{S}^{n-1}} \sum_{i=1}^{n} \sum_{j=i+1}^{n} \mathcal{C}(\boldsymbol{s}_i, k_i, \boldsymbol{s}_j, k_j) \mathcal{F}_n^{\vec{k}_n}(t, \vec{s}_n)\, d\vec{s}_n^{(2)}. \tag{B1}$$

For $i > 1$, each individual term appears once in the positive sum and once in the negative sum; they thus cancel each other out. The remaining terms are

$$\sum_{n=0}^{\infty} n \sum_{\vec{k}_n \in K_{2,n}} \int_{\mathbb{S}^{n-1}} \sum_{j=2}^{n} \mathcal{C}(\boldsymbol{s}_1, k_1 - 1, \boldsymbol{s}_j, k_j - 1) \mathcal{F}_n^{\vec{k}_{n,-}^{ij}}(t, \vec{s}_n)\, d\vec{s}_n^{(2)} - \sum_{n=0}^{\infty} n \sum_{\vec{k}_n \in K_{2,n}} \int_{\mathbb{S}^{n-1}} \sum_{j=2}^{n} \mathcal{C}(\boldsymbol{s}_1, k_1, \boldsymbol{s}_j, k_j) \mathcal{F}_n^{\vec{k}_n}(t, \vec{s}_n)\, d\vec{s}_n^{(2)}. \tag{B2}$$

Because $\mathcal{F}_n^{\vec{k}_n}(t, \vec{s}_n)$ is invariant with respect to particle relabeling, we can relabel $(\boldsymbol{s}_j, k_j) \leftrightarrow (\boldsymbol{s}_2, k_2)$ in each term in the sum over j to obtain

$$\begin{aligned}
\sum_{n=0}^{\infty} n \sum_{\vec{k}_n \in K_{2,n}} \int_{\mathbb{S}^{n-1}} \sum_{j=2}^{n} \mathcal{C}(\boldsymbol{s}_1, k_1, \boldsymbol{s}_j, k_j) \mathcal{F}_n^{\vec{k}_n}(t, \vec{s}_n)\, d\vec{s}_n^{(2)} &= \sum_{n=0}^{\infty} n \sum_{\vec{k}_n \in K_{2,n}} \int_{\mathbb{S}^{n-1}} \sum_{j=2}^{n} \mathcal{C}(\boldsymbol{s}_1, k_1, \boldsymbol{s}_2, k_2) \mathcal{F}_n^{\vec{k}_n}(t, \vec{s}_n)\, d\vec{s}_n^{(2)} \\
&= \sum_{n=0}^{\infty} n(n-1) \sum_{k_2=0}^{\infty} \int_{\mathbb{S}} \mathcal{C}(\boldsymbol{s}_1, k_1, \boldsymbol{s}_2, k_2) \sum_{\vec{k}_n \in K_{3,n}} \int_{\mathbb{S}^{n-2}} \mathcal{F}_n^{\vec{k}_n}(t, \vec{s}_n)\, d\vec{s}_n^{(3)}\, d\boldsymbol{s}_2 \\
&= \sum_{k_2=0}^{\infty} \int_{\mathbb{S}} \mathcal{C}(\boldsymbol{s}_1, k_1, \boldsymbol{s}_2, k_2) u_{k_1,k_2}^{(2)}(t, \boldsymbol{s}_1, \boldsymbol{s}_2)\, d\boldsymbol{s}_2\,,
\end{aligned}$$

where the last line follows from Eq. (14). Consequently, we can write (B1) as

$$\int_{\mathbb{S}} \sum_{k_2=0}^{\infty} \mathcal{C}(\boldsymbol{s}_1, k_1 - 1, \boldsymbol{s}_2, k_2 - 1) u_{k_1-1,k_2-1}^{(2)}(t, \boldsymbol{s}_1, \boldsymbol{s}_2)\, d\boldsymbol{s}_2 - \int_{\mathbb{S}} \sum_{k_2=0}^{\infty} \mathcal{C}(\boldsymbol{s}_1, k_1, \boldsymbol{s}_2, k_2) u_{k_1,k_2}^{(2)}(t, \boldsymbol{s}_1, \boldsymbol{s}_2)\, d\boldsymbol{s}_2\,. \tag{B3}$$

For the remaining terms on the RHS of Eq. (7), we sum over the degrees and integrate over the states of particles 2 through n, multiply by n, and sum over n to obtain

$$\sum_{n=1}^{\infty} n \sum_{\vec{k}_n \in K_{2,n}} \int_{\mathbb{S}^{n-1}} \left[\sum_{i=1}^{n} \frac{1}{n} \delta_{k_i,0}\, \mathcal{J}\, \mathcal{P}(\boldsymbol{s}_i) \mathcal{F}_{n-1}^{\vec{k}_n^{i-}}\left(t, \vec{s}_n^{i-}\right) - \mathcal{J} \mathcal{F}_n^{\vec{k}_n}(t, \vec{s}_n) \right] d\vec{s}_n^{(2)}. \tag{B4}$$

For the term $i = 1$, we are summing and integrating over all arguments of $\mathcal{F}_{n-1}^{\vec{k}_n^{i-}}(t, \vec{s}_n^{i-})$, so

$$\begin{aligned}
\sum_{n=1}^{\infty} n \sum_{\vec{k}_n \in K_{2,n}} \int_{\mathbb{S}^{n-1}} \frac{1}{n} \delta_{k_1,0}\, \mathcal{J}\, \mathcal{P}(\boldsymbol{s}_1) \mathcal{F}_{n-1}^{\vec{k}_n^{1-}}\left(t, \vec{s}_n^{1-}\right) d\vec{s}_n^{(2)} &= \delta_{k_1,0}\, \mathcal{J}\, \mathcal{P}(\boldsymbol{s}_1) \sum_{n=1}^{\infty} \sum_{\vec{k}_n \in K_{2,n}} \int_{\mathbb{S}^{n-1}} \mathcal{F}_{n-1}^{\vec{k}_n^{1-}}\left(t, \vec{s}_n^{1-}\right) d\vec{s}_n^{(2)} \\
&= \delta_{k_1,0}\, \mathcal{J}\, \mathcal{P}(\boldsymbol{s}_1) \sum_{n=1}^{\infty} \sum_{\vec{k}_{n-1} \in K_{1,n-1}} \int_{\mathbb{S}^{n-1}} \mathcal{F}_{n-1}^{\vec{k}_{n-1}}(t, \vec{s}_{n-1})\, d\vec{s}_{n-1} \\
&= \delta_{k_1,0}\, \mathcal{J}\, \mathcal{P}(\boldsymbol{s}_1)\,,
\end{aligned}$$

where the last line follows from Eq. (5). For each term $i > 1$, we use the invariance of $\mathcal{F}_n^{\vec{k}_n}(t, \vec{s}_n)$ with respect to particle relabeling to swap particle i with particle n to give

$$\begin{aligned}
&\sum_{n=1}^{\infty} n \sum_{\vec{k}_n \in K_{2,n}} \int_{\mathbb{S}^{n-1}} \sum_{i=2}^{n} \frac{1}{n} \delta_{k_i,0}\, \mathcal{J}\, \mathcal{P}(\boldsymbol{s}_i) \mathcal{F}_{n-1}^{\vec{k}_n^{i-}}\left(t, \vec{s}_n^{i-}\right) d\vec{s}_n^{(2)} \\
&= \sum_{n=1}^{\infty} n \sum_{\vec{k}_n \in K_{2,n}} \int_{\mathbb{S}^{n-1}} \sum_{i=2}^{n} \frac{1}{n} \delta_{k_n,0}\, \mathcal{J}\, \mathcal{P}(\boldsymbol{s}_n) \mathcal{F}_{n-1}^{\vec{k}_n^{n-}}\left(t, \vec{s}_n^{n-}\right) d\vec{s}_n^{(2)}
\end{aligned}$$

$$= \mathcal{J}\sum_{n=1}^{\infty}(n-1)\int_{\mathbb{S}}\mathcal{P}(\boldsymbol{s}_n)\,d\boldsymbol{s}_n\sum_{\vec{k}_{n-1}\in K_{1,n-1}}\int_{\mathbb{S}^{n-2}}\mathcal{F}_{n-1}^{\vec{k}_{n-1}}(t,\vec{s}_{n-1})\,d\vec{s}_{n-1}^{(2)}$$

$$= \mathcal{J}\sum_{n=0}^{\infty}n\sum_{\vec{k}_n\in K_{1,n}}\int_{\mathbb{S}^{n-1}}\mathcal{F}_{n}^{\vec{k}_n}(t,\vec{s}_n)\,d\vec{s}_n^{(2)},$$

which cancels with the remaining term in (B4).

APPENDIX C: ADDITIONAL DETAILS OF THE MODEL DERIVATION: EDGE DELETION

In kinetic theory, the first question to address when deriving a reduced model is which variables to retain in the model and which to integrate over. In Sec. IV, each variable was associated with a node in a network, and it was natural to integrate over all nodes but the first. We thus retained the state and degree of node 1 as independent variables. We could have reduced the model further by subsequently integrating over either the state or degree of node 1.

When considering edge deletion, it is much more difficult to associate the independent variables with individual nodes, and each entry of an adjacency matrix is associated with a pair of nodes. Consequently, it is not obvious which variables are natural to retain in a reduced model and which variables should be integrated out. To facilitate a direct comparison of the reduced model including edge deletion with the reduced model of Sec. IV, we again retain the state and degree of node 1 as independent variables. We thus sum over all entries of the adjacency matrix for which node 1 has degree k_1. Additionally, as before, we integrate over $\boldsymbol{s}_n^{(2)}$, multiply by n, and sum over n.

Because the operators $\mathcal{L}^{(n)}$ that we are considering do not depend on network structure, the approximation of the LHS of Eq. (23) proceeds as in Sec. IV B. For the edge-creation term on the RHS of Eq. (23), we find, as in Appendix B, that for $i>1$, each term appears once in the positive sum and once in the negative sum; these terms thus cancel. For the remaining terms (for which $i=1$), we exploit the invariance of $\mathscr{F}_n^{A_n}(t,\vec{s}_n)$ with respect to particle relabeling. Specifically, we relabel $j\leftrightarrow 2$ in each term in the sum over j (i.e., swapping rows and columns of A_n) to obtain

$$\sum_{n=0}^{\infty}n\sum_{A_n\in S_n}\int_{\mathbb{S}^{n-1}}\delta\left(k_1,\sum_{j=2}^{n}(A_n)_{1j}\right)(n-1)\mathcal{C}(\boldsymbol{s}_1,k_1-1,\boldsymbol{s}_2,k_2-1)\mathscr{F}_n^{A_{n,-}^{12}}(t,\vec{s}_n)\,d\vec{s}_n^{(2)}$$
$$-\sum_{n=0}^{\infty}n\sum_{A_n\in S_n}\int_{\mathbb{S}^{n-1}}\delta\left(k_1,\sum_{j=2}^{n}(A_n)_{1j}\right)(n-1)\mathcal{C}(\boldsymbol{s}_1,k_1,\boldsymbol{s}_2,k_2)\mathscr{F}_n^{A_n}(t,\vec{s}_n)\,d\vec{s}_n^{(2)}, \tag{C1}$$

where the Kronecker delta δ enforces the degree condition. The two-particle LSDD is

$$u_{k_1,k_2}^{(2)}(t,\boldsymbol{s}_1,\boldsymbol{s}_2)=\sum_{n=0}^{\infty}n(n-1)\sum_{A_n\in S_n}\delta\left(k_1,\sum_{j=2}^{n}(A_n)_{1j}\right)\delta\left(k_2,(A_n)_{12}+\sum_{j=3}^{n}(A_n)_{2j}\right)\int_{\mathbb{S}^{n-2}}\mathscr{F}_n^{A_n}(t,\vec{s}_n)\,d\vec{s}_n^{(3)}, \tag{C2}$$

so one can write (C1) as (B3), and the analysis proceeds as in Appendix B.

Let's now consider the edge-deletion terms. As with the edge-creation terms, for $i>1$, each term appears once in the positive sum and once in the negative sum; these terms thus cancel each other. For the remaining terms (for which $i=1$), relabeling $j\leftrightarrow 2$ in each term in the sum over j yields

$$\sum_{n=0}^{\infty}n(n-1)\sum_{A_n\in S_n}\delta\left(k_1,\sum_{j=2}^{n}(A_n)_{1j}\right)\int_{\mathbb{S}^{n-1}}[(A_n)_{12}+1]\mathcal{D}(\boldsymbol{s}_1,k_1+1,\boldsymbol{s}_2,k_2+1)\mathscr{F}_n^{A_{n,+}^{12}}(t,\vec{s}_n)\,d\vec{s}_n^{(2)}$$
$$-\sum_{n=0}^{\infty}n(n-1)\sum_{A_n\in S_n}\delta\left(k_1,\sum_{j=2}^{n}(A_n)_{1j}\right)\int_{\mathbb{S}^{n-1}}(A_n)_{12}\mathcal{D}(\boldsymbol{s}_1,k_1,\boldsymbol{s}_2,k_2)\mathscr{F}_n^{A_n}(t,\vec{s}_n)\,d\vec{s}_n^{(2)}$$
$$=\sum_{k_2=0}^{\infty}\int_{\mathbb{S}}\mathcal{D}(\boldsymbol{s}_1,k_1+1,\boldsymbol{s}_2,k_2+1)U_{k_1+1,k_2+1}^{(2)}(t,\boldsymbol{s}_1,\boldsymbol{s}_2)\,d\boldsymbol{s}_s-\sum_{k_2=0}^{\infty}\int_{\mathbb{S}}\mathcal{D}(\boldsymbol{s}_1,k_1,\boldsymbol{s}_2,k_2)U_{k_1,k_2}^{(2)}(t,\boldsymbol{s}_1,\boldsymbol{s}_2)\,d\boldsymbol{s}_s\,, \tag{C3}$$

where

$$U_{k_1,k_2}^{(2)}(t,\boldsymbol{s}_1,\boldsymbol{s}_2)=\sum_{n=0}^{\infty}n(n-1)\sum_{A_n\in S_n}\delta\left(k_1,\sum_{j=2}^{n}(A_n)_{1j}\right)\delta\left(k_2,(A_n)_{12}+\sum_{j=3}^{n}(A_n)_{2j}\right)\int_{\mathbb{S}^{n-2}}(A_n)_{12}\mathscr{F}_n^{A_n}(t,\vec{s}_n)\,d\vec{s}_n^{(3)}. \tag{C4}$$

There is now a new closure problem, as we need to relate $U^{(2)}_{k_1,k_2}(t,\boldsymbol{s}_1,\boldsymbol{s}_2)$ to known variables. We write

$$U^{(2)}_{k_1,k_2}(t,\boldsymbol{s}_1,\boldsymbol{s}_2) = \nu\, u^{(2)}_{k_1,k_2}(t,\boldsymbol{s}_1,\boldsymbol{s}_2)\,,$$

where ν is the expected number of edges between nodes 1 and 2, given that these nodes have degrees k_1 and k_2, respectively. If there are m edges in total, there are $2m$ stubs, of which k_1 are at node 1 and k_2 at node 2. One can approximate the probability that a given edge connects nodes 1 and 2 as

$$2 \times \frac{k_1}{2m} \times \frac{k_2}{2m},$$

so a reasonable closure assumption (reminiscent of a configuration model and hence with similar associated assumptions [97]) for the expected number of edges between nodes 1 and 2 is

$$\nu \approx \frac{k_1 k_2}{2m} = \frac{k_1 k_2}{E[N]\langle k\rangle} = \frac{k_1 k_2}{\int_{\mathbb{S}} \sum_{k_1=0}^{\infty} k_1 u_{k_1}(t,\boldsymbol{s}_1)\, d\boldsymbol{s}_1}\,,$$

where $E[N]$ is the expected number of nodes and $\langle k\rangle$ is the mean degree. Using a mean-field approximation for $u^{(2)}_{k_1,k_2}(t,\boldsymbol{s}_1,\boldsymbol{s}_2)$, we can then close the edge-deletion term by writing

$$U^{(2)}_{k_1,k_2}(t,\boldsymbol{s}_1,\boldsymbol{s}_2) = \frac{k_1 k_2 u_{k_1}(t,\boldsymbol{s}_1) u_{k_2}(t,\boldsymbol{s}_2)}{\int_{\mathbb{S}} \sum_{k_1=0}^{\infty} k_1 u_{k_1}(t,\boldsymbol{s}_1)\, d\boldsymbol{s}_1}\,.$$

Finally, we consider the node-creation term. The term $i = 1$ gives

$$\sum_{n=0}^{\infty} n \sum_{A_n \in S_n} \int_{\mathbb{S}^{n-1}} \delta\left(k_1, \sum_{j=2}^{n} (A_n)_{1j}\right) \frac{1}{n} \left[\prod_{j=2}^{n} \delta(0,(A_n)_{1j})\right] \mathcal{J}\mathcal{P}(\boldsymbol{s}_1) \mathscr{F}^{A_n^{1-}}_{n-1}\left(t,\vec{s}_n^{\,1-}\right) d\vec{s}_n^{\,(2)}$$

$$= \delta_{k_1,0}\, \mathcal{J}\, \mathcal{P}(\boldsymbol{s}_1) \sum_{n=1}^{\infty} \sum_{A_n^{1-} \in S_{n-1}} \int_{\mathbb{S}^{n-1}} \mathscr{F}^{A_n^{1-}}_{n-1}(t,\vec{s}_{n-1})\, d\vec{s}_{n-1} = \delta_{k_1,0}\, \mathcal{J}\, \mathcal{P}(\boldsymbol{s}_1)\,,$$

where the last equality follows by Eq. (20). For each term with $i > 1$, we can use the invariance of $\mathcal{F}^{\vec{k}_n}_n(t,\vec{s}_n)$ with respect to particle relabeling to swap particle i with particle n. As in our prior calculations, we then find that all of these terms cancel each other out.

[1] M. E. J. Newman, *Networks: An Introduction* (Oxford University Press, Oxford, UK, 2010).

[2] R. K. Jain, Determinants of tumor blood flow: A review, Cancer Res. **48**, 2641 (1988).

[3] B. Blonder, C. Violle, L. P. Bentley, and B. J. Enquist, Venation networks and the origin of the leaf economics spectrum, Ecol. Lett. **14**, 91 (2011).

[4] L. L. M. Heaton, E. López, P. K. Maini, M. D. Fricker, and N. S. Jones, Growth-induced mass flows in fungal networks, Proc. R. Soc. B: Biol. Sci. **277**, 3265 (2010).

[5] S. H. Lee, M. D. Fricker, and M. A. Porter, Mesoscale analyses of fungal networks as an approach for quantifying phenotypic traits, J. Complex Netw. **5**, 145 (2017).

[6] R. D. O'Dea, H. M. Byrne, and S. L. Waters, Continuum modelling of in vitro tissue engineering: A review, in *Computational Modeling in Tissue Engineering*, Studies in Mechanobiology, Tissue Engineering and Biomaterials, edited by L. Geris (Springer-Verlag, Cham, Switzerland, 2013), pp. 229–266.

[7] D. Hu and D. Cai, Adaptation and Optimization of Biological Transport Networks, Phys. Rev. Lett. **111**, 138701 (2013).

[8] J. Haskovec, P. Markowich, and B. Perthame, Mathematical analysis of a PDE system for biological network formation, Comm. Partial Differential Equations **40**, 918 (2015).

[9] G. Szabó and G. Fáth, Evolutionary games on graphs, Phys. Rep. **446**, 97 (2007).

[10] J. M. Smith, *Evolution and the Theory of Games* (Cambridge University Press, Cambridge, UK, 1982).

[11] M. Archetti, Evolutionary game theory of growth factor production: Implications for tumour heterogeneity and resistance to therapies, Br. J. Cancer **109**, 1056 (2013).

[12] H. Ohtsuki, C. Hauert, E. Lieberman, and M. A. Nowak, A simple rule for the evolution of cooperation on graphs and social networks, Nature (London) **441**, 502 (2006).

[13] M. Barthélemy, Spatial networks, Phys. Rep. **499**, 1 (2011).

[14] J. Lang, H. De Sterck, J. L. Kaiser, and J. C. Miller, Random spatial networks: Small worlds without clustering, traveling waves, and hop-and-spread disease dynamics, arXiv:1702.01252.

[15] R. Durrett and S. Levin, The importance of being discrete (and spatial), Theor. Popul. Biol. **46**, 363 (1994).

[16] R. Gallotti and M. Barthelemy, Anatomy and efficiency of urban multimodal mobility, Sci. Rep. **4**, 6911 (2014).

[17] R. Louf and M. Barthelemy, How congestion shapes cities: From mobility patterns to scaling, Sci. Rep. **4**, 5561 (2014).

[18] M. Barthelemy, *Morphogenesis of Spatial Networks* (Springer-Verlag, Cham, Switzerland, 2018).

[19] P. R. Buenzli, Osteocytes as a record of bone formation dynamics: A mathematical model of osteocyte generation in bone matrix, J. Theor. Biol. **364**, 418 (2015).

[20] S. L. Dallas and L. F. Bonewald, Dynamics of the transition from osteoblast to osteocyte, Ann. NY Acad. Sci. **1192**, 437 (2010).

[21] T. A. Franz-Odendaal, B. K. Hall, and P. E. Witten, Buried alive: How osteoblasts become osteocytes, Dev. Dyn. **235**, 176 (2006).

[22] Y. Ishihara, Y. Sugawara, H. Kamioka, N. Kawanabe, H. Kurosaka, K. Naruse, and T. Yamashiro, In situ imaging of the autonomous intracellular Ca^{2+} oscillations of osteoblasts and osteocytes in bone, Bone **50**, 842 (2012).

[23] P. Kollmannsberger, M. Kerschnitzki, F. Repp, W. Wagermaier, R. Weinkamer, and P. Fratzl, The small world of osteocytes: Connectomics of the lacuno-canalicular network in bone, arXiv:1702.04117.

[24] M. Penrose, *Random Geometric Graphs* (Oxford University Press, Oxford, UK, 2003).

[25] D. J. de Solla Price, *Little Science, Big Science and Beyond* (Columbia University Press, New York, NY, USA, 1986).

[26] C. Moore, G. Ghoshal, and M. E. J. Newman, Exact solutions for models of evolving networks with addition and deletion of nodes, Phys. Rev. E **74**, 036121 (2006).

[27] P. L. Krapivsky, G. J. Rodgers, and S. Redner, Degree Distributions of Growing Networks, Phys. Rev. Lett. **86**, 5401 (2001).

[28] P. L. Krapivsky and S. Redner, Organization of growing random networks, Phys. Rev. E **63**, 066123 (2001).

[29] T. Gross and B. Blasius, Adaptive coevolutionary networks: A review, J. R. Soc. Interface **5**, 259 (2008).

[30] K. Zuev, M. Boguña, G. Bianconi, and D. Krioukov, Emergence of soft communities from geometric preferential attachment, Sci. Rep. **5**, 9421 (2015).

[31] P. L. Krapivsky, S. Redner, and E. Ben-Naim, *A Kinetic View of Statistical Physics* (Cambridge University Press, Cambridge, UK, 2010).

[32] V. Marceau, P.-A. Noël, L. Hébert-Dufresne, A. Allard, and L. J. Dubé, Adaptive networks: Coevolution of disease and topology, Phys. Rev. E **82**, 036116 (2010).

[33] M. Boguñá, R. Pastor-Satorras, A. Díaz-Guilera, and A. Arenas, Emergence of clustering, correlations, and communities in a social network model, arXiv:cond-mat/0309263.

[34] L. H. Wong, P. Pattison, and G. Robins, A spatial model for social networks, Physica A **360**, 99 (2006).

[35] J. Barré, J. A. Carrillo de la Plata, P. Degond, D. Peurichard, and E. Zatorska, Particle interactions mediated by dynamical networks: Assessment of macroscopic descriptions, arXiv:1701.01435 (2017).

[36] More precisely, $f(t,\boldsymbol{s})\,d\boldsymbol{s}$ gives the expected number of particles that have states lying in the volume element $d\boldsymbol{s}$ centered on $\boldsymbol{s}$.

[37] P. Degond, L. Pareschi, and G. Russo, *Modeling and Computational Methods for Kinetic Equations* (Birkhäuser, Basel, Switzerland, 2004).

[38] I. Gallagher, L. Saint-Raymond, and B. Texier, *From Newton to Boltzmann: Hard Spheres and Short-Range Potentials* (American Mathematical Society, Providence, RI, USA, 2014).

[39] R. Illner and M. Pulvirenti, A derivation of the BBGKY-hierarchy for hard-sphere particle systems, Transport Theory Stat. Phys. **16**, 997 (1987).

[40] Following standard practice, we use capital letters for random variables and lower-case letters for realizations of these variables.

[41] B. Øksendal, *Stochastic Differential Equations: An Introduction with Applications (Universitext)*, 6th ed. (Springer-Verlag, Cham, Switzerland, 2014).

[42] H. Othmer, S. R. Dunbar, and W. Alt., Models of dispersal in biological systems, J. Math. Biol. **26**, 263 (1988).

[43] R. Metzler and J. Klafter, The random walk's guide to anomalous diffusion: A fractional dynamics approach, Phys. Rep. **339**, 1 (2000).

[44] M. Kivelä, A. Arenas, M. Barthelemy, J. P. Gleeson, Y. Moreno, and M. A. Porter, Multilayer networks, J. Complex Netw. **2**, 203 (2014).

[45] M. Bisi and L. Desvillettes, From reactive Boltzmann equations to reaction–diffusion systems, J. Stat. Phys. **124**, 881 (2006).

[46] J. M. Burgers, The Boltzmann equation for flows with chemical reactions, Planet. Space Sci. **3**, 4 (1961).

[47] W. Chen, R. Erban, and S. J. Chapman, From Brownian dynamics to Markov chain: An ion channel example, SIAM J Appl. Math. **74**, 208 (2014).

[48] J. A. Carrillo, M. R. D'Orsogna, and V. Panfarov, Double milling in self-propelled swarms from kinetic theory, Kinetic Related Models **2**, 363 (2009).

[49] C. Cercignani, *The Boltzmann Equation and Its Applications* (Springer-Verlag, New York, NY, USA, 1988).

[50] S. Harris, *An Introduction to the Theory of the Boltzmann Equation* (Holt, Reinhart and Winston, New York, NY, USA, 1971).

[51] M. Bruna and S. J. Chapman, Excluded-volume effects in the diffusion of hard spheres, Phys. Rev. E **85**, 011103 (2012).

[52] J. A. Peacock, Two-dimensional goodness-of-fit testing in astronomy, Mon. Not. R. Astron. Soc. **202**, 615 (1983).

[53] D. Krioukov and M. Ostilli, Duality between equilibrium and growing networks, Phys. Rev. E **88**, 022808 (2013).

[54] M. Boguñá and R. Pastor-Satorras, Class of correlated random networks with hidden variables, Phys. Rev. E **68**, 036112 (2003).

[55] T. Hillen, On the L^2-moment closure of transport equations: The general case, Discrete Con. Dyn. Syst. Series B **5**, 299 (2005).

[56] T. Hillen, On the L^2-moment closure of transport equations: The Cattaneo approximation, Discrete Contin. Dyna. Syst. Series B **4**, 961 (2004).

[57] C. Kuehn, Moment closure—A brief review, in *Control of Self-Organizing Nonlinear Systems*, edited by E. Schöll, S. H. L. Klapp, and P. Hövel (Springer-Verlag, Cham, Switzerland, 2016), pp. 253–271.

[58] M. L. K. Tate, J. R. Adamson, A. E. Tami, and T. W. Bauer, The osteocyte, Intl. J. Biochem. Cell Biol. **36**, 1 (2004).

[59] Y. Carter, J. L. Suchorab, C. D. L. Thomas, J. G. Clement, and D. M. L. Cooper, Normal variation in cortical osteocyte lacunar parameters in healthy young males, J. Anat. **225**, 328 (2014).

[60] A. Piattelli, L. Artese, E. Penitente, F. Iaculli, M. Degidi, C. Mangano, J. A. Shibli, P. G. Coelho, V. Perrotti, and G. Iezzi, Osteocyte density in the peri-implant bone of implants retrieved after different time periods (4 weeks to 27 years), J. Biomed. Mater. Res. Part B: Appl. Biomaterials **102**, 239 (2014).

[61] R. L. Jilka, B. Noble, and R. S. Weinstein, Osteocyte apoptosis, Bone **54**, 264 (2013).

[62] J. Xiong, M. Piemontese, J. D. Thostenson, R. S. Weinstein, S. C. Manolagas, and C. A. O'Brien, Osteocyte-derived RANKL is a critical mediator of the increased bone resorption caused by dietary calcium deficiency, Bone **66**, 146 (2014).

[63] R. Sapir-Koren and G. Livshits, Osteocyte control of bone remodeling: Is sclerostin a key molecular coordinator of the balanced bone resorption–formation cycles?, Osteoporosis Intl., **25**, 2685 (2014).

[64] M. Kerschnitzki, P. Kollmannsberger, M. Burghammer, G. N. Duda, R. Weinkamer, W. Wagermaier, and P. Fratzl, Architecture of the osteocyte network correlates with bone material quality, J. Bone Miner. Res. **28**, 1837 (2013).

[65] H. Kamioka, T. Honjo, and T. Takano-Yamamoto, A three-dimensional distribution of osteocyte processes revealed by the combination of confocal laser scanning microscopy and differential interference contrast microscopy, Bone **28**, 145 (2001).

[66] Y. Sugawara, R. Ando, H. Kamioka, Y. Ishihara, T. Honjo, N. Kawanabe, H. Kurosaka, T. Takano-Yamamoto, and T. Yamashiro, The three-dimensional morphometry and cell–cell communication of the osteocyte network in chick and mouse embryonic calvaria, Calcif. Tissue Int. **88**, 416 (2011).

[67] Y. Sugawara, H. Kamioka, T. Honjo, K. ichi Tezuka, and T. Takano-Yamamoto, Three-dimensional reconstruction of chick calvarial osteocytes and their cell processes using confocal microscopy, Bone **36**, 877 (2005).

[68] P. R. Buenzli and N. A. Sims, Quantifying the osteocyte network in the human skeleton, Bone **75**, 144 (2015).

[69] Creative Commons BY-NC-ND 4.0, https://creativecommons.org/licenses/by-nc-nd/4.0/.

[70] Wellcome Images., http://wellcomeimages.org. Copyrighted work available under Creative Commons from Kevin Mackenzie, University of Aberdeen (B0008430).

[71] A. G. Robling, A. B. Castillo, and C. H. Turner, Biomechanical and molecular regulation of bone remodeling, Annu. Rev. Biomed. Eng. **8**, 455 (2006).

[72] O. D. Kennedy, D. M. Laudier, R. J. Majeska, H. B. Sun, and M. B. Schaffler, Osteocyte apoptosis is required for production of osteoclastogenic signals following bone fatigue *in vivo*, Bone **64**, 132 (2014).

[73] The unit that consists of osteoblasts following osteoclasts is known as a "bone multicellular unit" (BMU).

[74] M. P. Roudier, L. D. True, C. S. Higano, H. Vesselle, W. Ellis, P. Lange, and R. L. Vessella, Phenotypic heterogeneity of end-stage prostate carcinoma metastatic to bone, Human Pathol. **34**, 646 (2003).

[75] X. H.-F. Zhang, X. Jin, S. Malladi, Y. Zou, Y. H. Wen, E. Brogi, M. Smid, J. A. Foekens, and J. Massagué, Selection of bone metastasis seeds by mesenchymal signals in the primary tumor stroma, Cell **154**, 1060 (2013).

[76] P. Pivonka and S. V. Komarova, Mathematical modeling in bone biology: From intracellular signaling to tissue mechanics, Bone **47**, 181 (2010).

[77] Y.-C. Lee, C.-J. Cheng, M. A. Bilen, J.-F. Lu, R. L. Satcher, L.-Y. Yu-Lee, G. E. Gallick, S. N. Maity, and S.-H. Lin, BMP4 promotes prostate tumor growth in bone through osteogenesis, Cancer Res. **71**, 5194 (2011).

[78] E. C. Connolly, J. Freimuth, and R. J. Akhurst, Complexities of TGF-β targeted cancer therapy, Intl. J. Biol. Sci. **8**, 964 (2012).

[79] J. M. Graham, B. P. Ayati, S. A. Holstein, and J. A. Martin, The role of osteocytes in targeted bone remodeling: A mathematical model, PLoS ONE **8**, e63884 (2013).

[80] A. Moroz, M. C. Crane, G. Smith, and D. I. Wimpenny, Phenomenological model of bone remodeling cycle containing osteocyte regulation loop, Biosystems **84**, 183 (2006).

[81] D. I. Wimpenny and A. Moroz, On allosteric control model of bone turnover cycle containing osteocyte regulation loop, Biosystems **90**, 295 (2007).

[82] M. D. Ryser, S. V. Komarova, and N. Nigam, The cellular dynamics of bone remodeling: A mathematical model, SIAM J. Appl. Math. **70**, 1899 (2010).

[83] M. D. Ryser, N. Nigam, and S. V. Komarova, Mathematical modeling of spatio-temporal dynamics of a single bone multicellular unit, J. Bone Miner. Res. **24**, 860 (2009).

[84] M. D. Ryser, Y. Qu, and S. V. Komarova, Osteoprotegerin in bone metastases: Mathematical solution to the puzzle, PLoS Comput. Biol. **8**, e1002703 (2012).

[85] K. A. Rejniak and A. R. A. Anderson, Hybrid models of tumor growth, Wiley Interdisc. Rev.: Syst. Biol. Med. **3**, 115 (2011).

[86] R. F. M. van Oers, J. Klein-Nulend, and R. l. G. Bacabac, The osteocyte as an orchestrator of bone remodeling: An engineer's perspective, Clin. Rev. Bone Mineral Metabolism **12**, 2 (2014).

[87] J. C. Stinson, The ailing mythical osteocyte, Med. Hypotheses **1**, 186 (1975).

[88] S. Eisenberger, K. Ackermann, G. Voggenreiter, H. Sültmann, C. Kasperk, and W. Pyerin, Metastases and multiple myeloma generate distinct transcriptional footprints in osteocytes in vivo, J. Pathol. **214**, 617 (2008).

[89] P. R. Buenzli, P. Pivonka, and D. W. Smith, Bone refilling in cortical basic multicellular units: Insights into tetracycline double labelling from a computational model, Biomech. Model. Mechanobiol. **13**, 185 (2014).

[90] G. Marotti, A. Z. Zallone, and M. Ledda, Number, size and arrangement of osteoblasts in osteons at different stages of formation, Calcif. Tissue Int. **21**, 96 (1975).

[91] K. M. Hannah, C. D. L. Thomas, J. G. Clement, F. De Carlo, and A. G. Peele, Bimodal distribution of osteocyte lacunar size in the human femoral cortex as revealed by micro-CT, Bone **47**, 866 (2010).

[92] A. Araujo, L. M. Cook, C. C. Lynch, and D. Basanta, An integrated computational model of the bone microenvironment in bone-metastatic prostate cancer, Cancer Res. **74**, 2391 (2014).

[93] C. J. Logothetis and S.-H. Lin, Osteoblasts in prostate cancer metastasis to bone, Nature Rev. Cancer **5**, 21 (2005).

[94] R. Bataille, D. Chappard, C. Marcelli, J.-F. Rossi, P. Dessauw, P. Baldet, J. Sany, and C. Alexandre, Osteoblast stimulation in multiple myeloma lacking lytic bone lesions, Br. J. Haematol. **76**, 484 (1990).

[95] D. J. Higham, An algorithmic introduction to numerical simulation of stochastic differential equations, SIAM Rev. **43**, 525 (2001).

[96] D. T. Gillespie, Exact stochastic simulation of coupled chemical reactions, J. Phys. Chem. **81**, 2340 (1977).

[97] B. K. Fosdick, D. B. Larremore, J. Nishimura, and J. Ugander, Configuring random graph models with fixed degree sequences, arXiv:1608.00607 [SIAM Review (to be published)].